

PAPER • OPEN ACCESS

Development and dosimetric evaluation of a modulated intraoperative radiotherapy (mIORT) system using the Zeiss intrabeam device

To cite this article: Xavier Jones *et al* 2025 *Phys. Med. Biol.* **70** 075012

View the [article online](#) for updates and enhancements.

You may also like

- [Evaluation of Ge-doped silica fibre TLDs for *in vivo* dosimetry during intraoperative radiotherapy](#)
F Moradi, N M Ung, G A Mahdiraji et al.
- [Monte Carlo simulation of electron beams generated by a 12 MeV dedicated mobile IORT accelerator](#)
G Iaccarino, L Strigari, M D'Andrea et al.
- [In vivo dosimetry in cancer patients undergoing intraoperative radiation therapy](#)
Anna Petoukhova, Roland Snijder, Thomas Vissers et al.



PAPER

OPEN ACCESS

RECEIVED
12 December 2024REVISED
7 February 2025ACCEPTED FOR PUBLICATION
13 March 2025PUBLISHED
25 March 2025

Original content from
this work may be used
under the terms of the
[Creative Commons
Attribution 4.0 licence](#).

Any further distribution
of this work must
maintain attribution to
the author(s) and the title
of the work, journal
citation and DOI.



Development and dosimetric evaluation of a modulated intraoperative radiotherapy (mIORT) system using the Zeiss intrabeam device

Xavier Jones^{1,*} , Gabor Neveri² , Marsha Chin³  and Pejman Rowshanfarzad^{1,4} ¹ School of Physics, Mathematics and Computing, The University of Western Australia, Crawley, WA 6009, Australia² Department of Radiation Oncology, Sir Charles Gairdner Hospital, Nedlands, WA, Australia³ Health Technology Management Unit, Royal Perth Hospital, Perth, WA 6000, Australia⁴ Centre for Advanced Technologies in Cancer Research (CATCR), Perth, WA 6000, Australia

* Author to whom any correspondence should be addressed.

E-mail: xavier.jones13701@gmail.com**Keywords:** intraoperative radiotherapy, Monte Carlo, intrabeam, dosimetry, modulation

Abstract

Objective. Intraoperative radiotherapy (IORT) is a specialised radiotherapy technique that delivers a precise, single high-dose fraction to the tumour bed after surgical removal of the tumour, aiming to eliminate residual cancer cells. This study investigates the incorporation of novel applicators into an existing IORT system to enable dose modulation, performing Monte Carlo (MC) simulations, 3D printing, and experimental validation. The Zeiss Intrabeam IORT device, a low-kV IORT system capable of delivering x-rays nearly isotropically, with energies up to 50 kV, was used in this study. **Approach.** Applicators were modified to alter dose distributions, incorporating features such as shielding or changes to an ellipsoid shape. The EGSnrc MC code was employed to simulate the dose distributions of each applicator design, generating data such as dose maps, percentage depth dose (PDD) curves, per cent difference maps between shielded and unshielded regions, and energy spectra to characterise each applicator. Gafchromic EBT3 film measurements were performed on select 3D printed applicators, to verify the MC simulations, with dose distribution data extracted for comparison. **Main Results.** Visual comparisons of dose and percentage different maps indicate a high correlation between the MC simulations and film measurements. Most PDD points for spherical applicators showed deviations within 4%, while ellipsoid applicators had deviations of 14% for the unshielded and 5% for the shielded applicators. All Root Mean Square Error (RMSEs) were below 0.05 for spherical and 0.18 for ellipsoid designs. Based on film data, shielded ellipsoid applicators reduced the dose by ~99%, 48%, 22%, and 8% at 0.3, 1, 2, and 3 cm, respectively, while shielded spherical applicators achieved ~83%, 35%, 14%, and 7% reductions at the same distances. Energy spectra for photons exiting shielded regions were also generated. **Significance.** Results of this study may be used in the development of patient-specific IORT techniques, or the development of a treatment planning system involving mIORT.

1. Introduction

Intraoperative radiotherapy (IORT) is a specialised radiotherapy technique involving delivering a precise, single fraction of high dose to a tumour bed after the tumour has been surgically removed. This aims to eliminate remaining cancer cells within the bed, preventing recurrence and improving the tumour control probability. Normal tissue is typically shielded or displaced out of the radiation field.

The Carl Zeiss Intrabeam is a low-kV IORT system that delivers x-rays from a source nearly isotropically. It consists of a central control console and the XRS unit. The console supplies a voltage to the XRS, specifically to its cathode gun, which generates a beam of electrons. These electrons travel through an acceleration drift tube, are guided by a beam deflector, and then pass into a probe. The XRS functions as a

miniaturized linear accelerator, where the electrons strike a gold target, producing Bremsstrahlung x-rays. The system allows for adjustable photon energies of 30, 40, or 50 kV, with currents of 5, 10, 20 or 40 μA (Gunderson *et al* 2011). Applicators, such as spherical, needle, flat, and surface designs offered by Zeiss, can be used to modify the dose distribution.

EGSnrc is a software toolkit used to execute MC simulations to model the interaction of ionising radiation with matter. EGSnrc models the propagation of photons, electrons and positrons with kinetic energies ranging from 1 keV to 10 GeV in homogeneous materials. The toolkit includes the `egs++` class library, a C++ library, which allows the modelling of complex geometries and particle sources. Other components integrated into the software include BEAMnrc, which contains the utility DOSXYZnrc for dose scoring, allowing for radiation dose estimations in voxel geometries, among other data processing tools for beam characteristic analysis and the generation of dose profiles (Kawrakow *et al* 2000, 2023).

The Zeiss recommended method for dosimetry of the Intrabeam system involves using a soft x-ray parallel-plate ionisation chamber within the Zeiss water phantom. However, ionisation chambers provide one-dimensional data, whilst film measurements can provide high resolution two-dimensional data. Before the study performed by Chin *et al* (2023), there were few articles employing film dosimetry of the Zeiss Intrabeam system (Clausen *et al* 2012, Nwankwo *et al* 2013, Schneider *et al* 2014, Sethi *et al* 2018), and even fewer utilised film directly in water (Eaton and Duck 2010, Moradi *et al* 2017, Watson *et al* 2018). Using a laser cutter allows for greater precision and reproducibility when cutting film compared to scissors (Zolfaghari *et al* 2017). The slow water penetration rate of Gafchromic film makes dosimetry directly in water viable (Devic *et al* 2010).

Prior to the research by Chin *et al*'s (2023), several studies simulated the Intrabeam system using various MC toolkits (Ebert and Carruthers 2003, Clausen *et al* 2012, Nwankwo *et al* 2013, Bouzid *et al* 2015, Moradi *et al* 2017, Watson *et al* 2017, Alvarez *et al* 2020, Shamsabadi *et al* 2020, 2021, Ayala Alvarez *et al* 2021), while only a few utilised EGSnrc or included simulations of the spherical applicators. Chin *et al*'s (2023) study involved modelling the Zeiss Intrabeam system's bare probe and its spherical applicators, with model verification performed using ionisation chamber and Gafchromic film measurements in water. Although the results confirmed the device's characteristic steep dose gradient, studies on the effects of shielding and modifications to the applicator heads remain unexplored.

The aim of this study was to integrate novel applicators into an existing IORT system to enable dose modulation. A modulated IORT (mIORT) system was developed and evaluated dosimetrically using Monte Carlo (MC) simulations, 3D printing, and film measurements. By spatially varying dose intensity to the tumour bed, mIORT aimed to improve dose conformity while sparing healthy tissue and critical structures, thereby reducing normal tissue complications and enhancing the therapeutic ratio, and providing a foundation for patient-specific IORT in the future.

2. Materials and methods

2.1. MC simulations

The 2023 release version of EGSnrc was used for MC simulations (Kawrakow *et al* 2000). The MC models employed in this study are either exact copies or modified versions of models previously developed by Chin *et al* (2023). The bare probe model consists of a 10 cm long, 3.2 mm diameter tube made of μ -metal, except for the distal 1.6 cm beryllium exit window. Outer layers of 2.5 μm thick NiO, Ni and CrN line the probe, whilst a 1 μm thick gold target lines the distal interior. The electron source was modelled with a Gaussian energy distribution, having a mean energy of 50 keV and FWHM of 5 keV, in accordance with vendor specification (Clausen *et al* 2012). The electron beam consists of two rings with radii of 0.6–0.7 mm and 0.7–0.8 mm, with corresponding weighting factors of 1.05 and 1.55, as determined by Clausen *et al* (2012). Eight spherical applicators, consisting of a shank and a ball with diameters ranging from 1.5 to 5 cm in 0.5 cm increments, were also modelled by Chin *et al* (2023). These applicators are made of polyetherimide, with applicators of diameters 1.5–3 cm containing an additional aluminium layer.

In this study, modifications were made to the structure of the 3.5 cm diameter spherical applicator head to facilitate modulated IORT (mIORT), and to the applicator material. The 3.5 cm applicator was selected because it is the smallest size without an aluminium layer, simplifying subsequent 3D printing.

The applicator material was changed from polyetherimide (used commercially (AG CZM 2022)) to FormFutura Volcano PLA (FormFutura 2024), a high-density version of regular PLA ($\text{C}_3\text{H}_4\text{O}_2$)_n, with density of 1.27 gcm^{-3} (FormFutura 2019). This change was due to limitations in 3D printing polyetherimide with the available printers. The recommended print settings (FormFutura 2024) indicate the need for an industrial-grade printer, which was not accessible during the study. Volcano PLA was chosen based on its availability and its properties, which are as close to polyetherimide as possible based on CT number. As this is

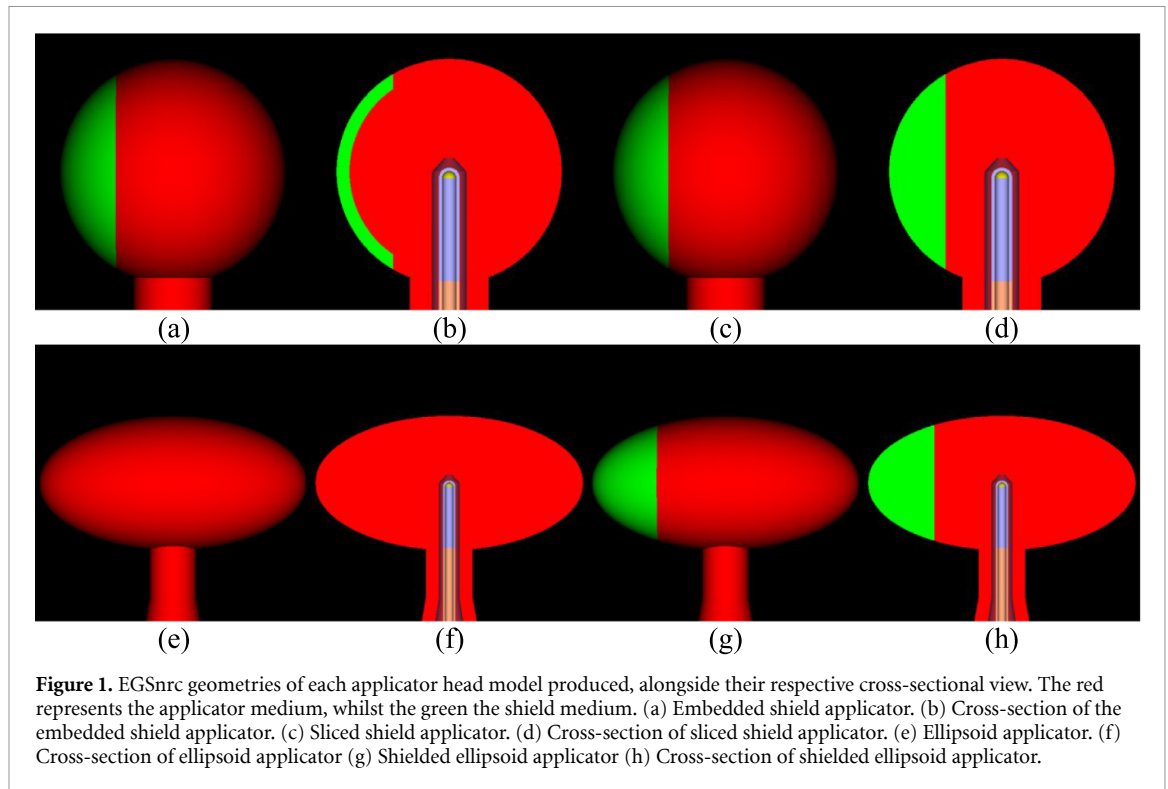


Figure 1. EGSnrc geometries of each applicator head model produced, alongside their respective cross-sectional view. The red represents the applicator medium, whilst the green the shield medium. (a) Embedded shield applicator. (b) Cross-section of the embedded shield applicator. (c) Sliced shield applicator. (d) Cross-section of sliced shield applicator. (e) Ellipsoid applicator. (f) Cross-section of ellipsoid applicator (g) Shielded ellipsoid applicator (h) Cross-section of shielded ellipsoid applicator.

Table 1. Embedded shield variables and their corresponding values used for EGSnrc simulations. The ‘distance from midpoint’ variable refers to the starting position of the shield, expressed as a fraction of the distance between the midpoint and the outer sphere radius. Shield thicknesses of 0.05 mm and 0.1 mm were exclusively produced for tungsten and tungsten filament media shields at 1/2 distance from the midpoint and 0° angle. Shields angled at 45° from the sphere’s central cross-sectional Z-plane were exclusively created for tungsten and tungsten filament shields.

Variable	Value
Shield thickness (mm)	0.05, 0.1, 0.5, 1, 2
Distance from midpoint (as a fraction between midpoint and sphere radius)	1/2, 3/4
Angle (°)	0, 45
Material	Tungsten, tungsten filament, gold, lead, copper, aluminium

Table 2. Sliced shield variables and their corresponding values used for EGSnrc simulations. The ‘distance from midpoint’ variable refers to the starting position of the shield, expressed as a fraction of the distance between the midpoint and the outer sphere radius. A value of 0/4 indicates that the shield begins at the sphere’s midpoint. Shields angled at 45° from the sphere’s central cross-sectional Z-plane were exclusively created for tungsten and tungsten filament shields.

Variable	Value
Distance From Midpoint (as a fraction between midpoint and sphere radius)	0/4, 1/4, 2/4, 3/4
Angle (°)	0, 45
Material	Tungsten, tungsten filament, gold, lead, copper, aluminium

a proof-of-concept study, this material substitution was feasible, and the MC models were updated to reflect the use of Volcano PLA for comparison with physical measurements produced later.

For investigating mIORT techniques, modifications were made to the applicator head design. The first design included a shield ‘embedded’ into the head of the applicator, as shown in figures 1(a) and (b). Multiple models with varying shield parameters were created, as detailed in table 1.

Models of applicators with ‘slices’ of the ball replaced with shield media were created, depicted in figures 1(c) and (d). The shield variables used for the different models are detailed in table 2.

A model of an applicator with an ellipsoid-shaped head, instead of a spherical one, was produced. The ellipsoid was created using the `egs++ conestack` geometry, and the ellipse equation:

$$\frac{x^2}{a^2} + \frac{y^2}{b^2} = 1. \quad (1)$$

Table 3. Shielded ellipsoid variables and their corresponding values used for EGSnrc simulations. The ‘distance from midpoint’ variable refers to the starting position of the shield, expressed as a percentage of the distance between the ellipsoid’s midpoint and its long axis radius.

Variable	Value
Distance from midpoint (as a fraction between midpoint and sphere radius)	1/10, 1/4, 1/2, 3/4, 9/10
Material	Tungsten, tungsten filament, gold, lead, copper, aluminium

The ellipsoid was approximated as a series of 198 frustums. In this study, a single ellipsoid size was used, with short- and long-axis radii of 1.75 and 3.5 cm, respectively. This is shown in figures 1(e) and (f).

Ellipsoid applicator models with slices replaced by shield media were also created. Multiple shield variables were used, as detailed in table 3. Figures 1(g) and (h) illustrate an example of these shielded ellipsoid models.

The tungsten filament mentioned refers to a Rapid 3DShield tungsten filament (The Virtual Foundry 2024), which will later be used in 3D printing. This filament is modelled here for comparison purposes and consists of 93.5% by weight tungsten powder embedded in 6.5% by weight PLA, with a density of 7.51 gcm^{-3} .

The applicator geometries were enveloped by and simulated in a $30 \text{ cm} \times 20 \text{ cm} \times 30 \text{ cm}$ prism water phantom with voxel sizes of $1.6 \text{ mm} \times 1.6 \text{ mm} \times 1 \text{ mm}$. The small voxel sizes allow for greater accuracy in determining the dose distribution in the steep fall-off regions characteristic of the applicators. `.3ddose` files were generated for each simulated model, recording the dose and associated error for each voxel. To determine energy spectra, phase space analysis was performed, scoring photons as they entered an X -plane just touching the outer surface of the shield. This analysis provides an indication of the spectra of photons leaving the shielded region of the applicator, which is the region of interest in this study.

Simulations were performed using an Intel® Xeon® CPU E5-2640 v2 @ 2.00GHZ processor with 32 cores & 125.8 GiB of memory, distributed across 30 parallel cores. A phase space was generated using Chin *et al* (2023)’s bare probe models, by combining five sets of phase spaces, each produced with 3×10^{10} histories. This phase space contained 2×10^8 particles and was used as the source for each subsequent applicator simulation. For simulations that produced `.3ddose` outputs, 10^{10} history simulations were performed, whilst 10^9 histories were used for the energy spectra phase space outputs. The minimum and maximum threshold energies for particle production were set at 521 keV and 700 keV for electrons, and 1 kV and 200 kV for photons, respectively. The electron and photon threshold energy for particle absorption were 521 keV and 1 kV, respectively. The electron energy includes its rest mass energy of 511 keV, and hence all electrons with energies less than 10 keV are absorbed in their current region. The choice of these parameters was based on the study by Chin *et al* (2023), with only slight modifications to improve performance.

Dose maps were generated in the central cross-sectional Z -plane of the applicators and normalised to their maximum dose within the plane. PDD curves were produced in the direction of the shields. To fit the MC data to a curve, the `curve_fit` function from the `scipy.optimize` Python sub-package was used which provided equation (2) as the optimal function (highest R2 value):

$$y = 100Ae^{-Bx} + 100Ce^{-Dx} \quad (2)$$

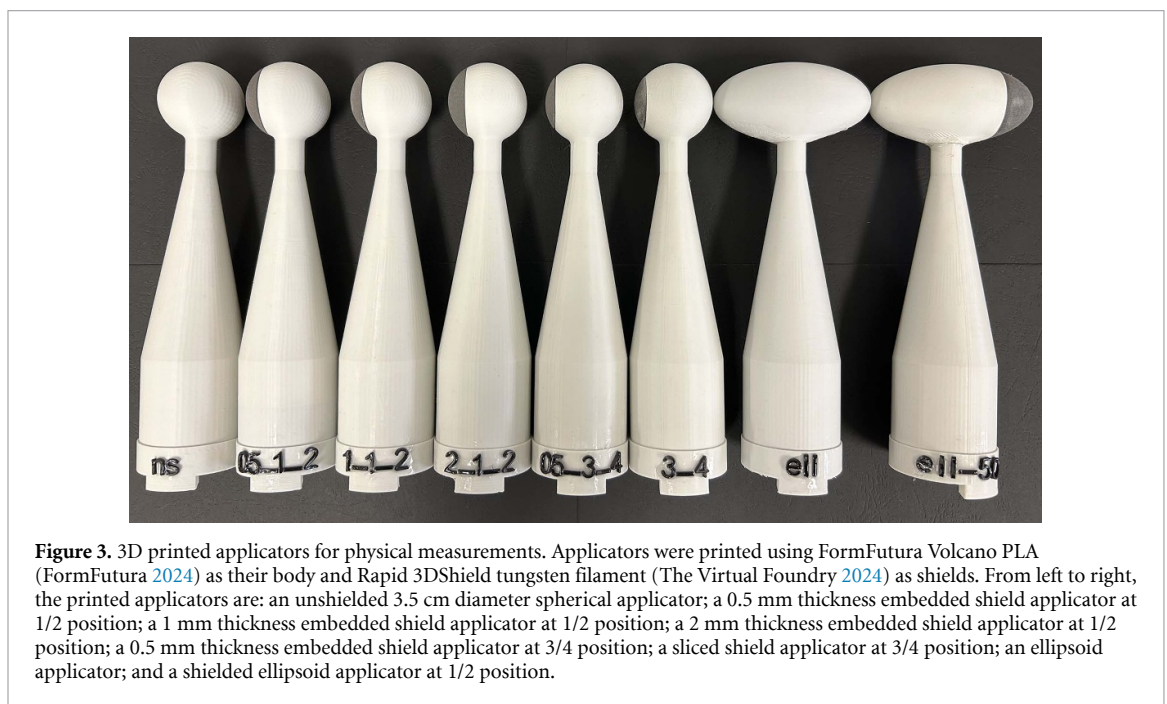
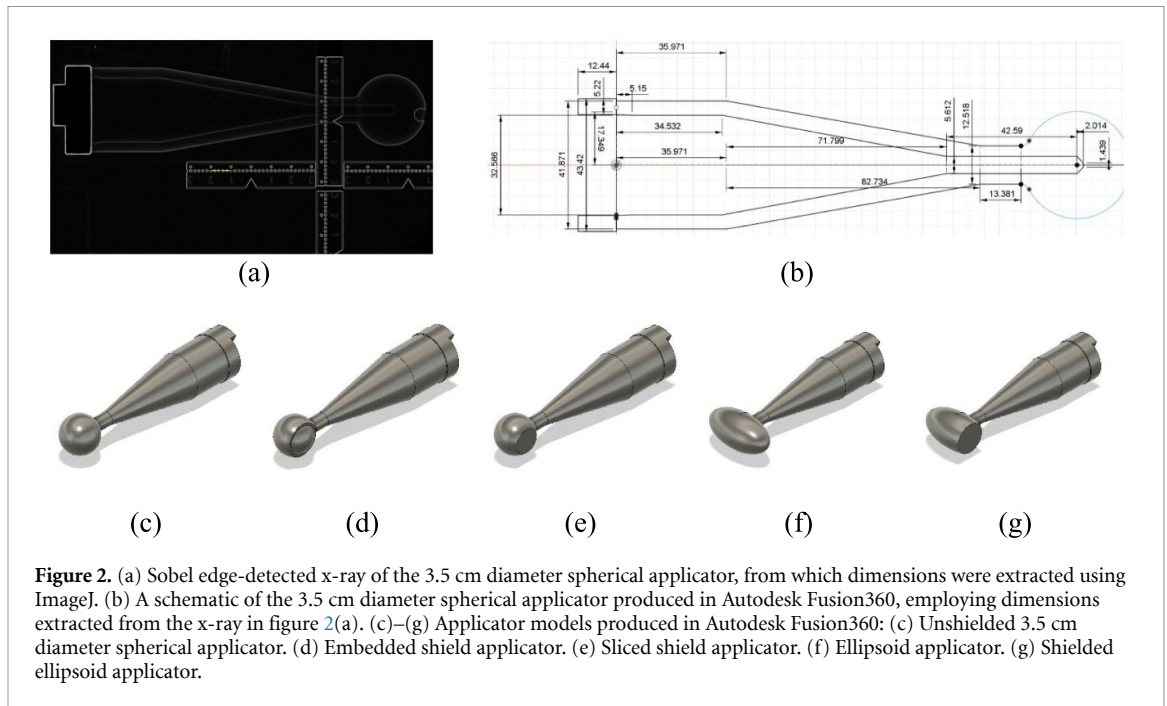
which provided the best fit for the data. Percentage difference plots comparing the dose distribution on the unshielded side of the applicators to that on the shielded side were also generated. Finally, energy spectra plots for each applicator were created using Python.

2.2. Physical modelling and 3D printing

A Sobel filter was applied to detect the edges of an x-ray image of the 3.5 cm applicator (figure 2(a)), previously produced by Chin *et al* (2022), and the extracted dimensions were used for 3D modelling. These dimensions were used to construct detailed models in AutoDesk Fusion360. A sketch showing the extracted dimensions is displayed in figure 2(b), which served as the basis for developing a model of the unshielded 3.5 cm applicator.

A model of the unshielded 3.5 cm applicator is displayed in figure 2(c). Modifications were applied to the head of this model to create the additional required models, as displayed in figures 2(d)–(g). These models were prepared for 3D printing and subsequent physical measurements. Although many models were simulated in EGSnrc, not all were intended for physical measurements. Nevertheless, all these models and their corresponding shields were developed in Fusion360.

A subset of models was selected for 3D printing and physical measurements. Their designs were exported from Fusion360 as `.stl` files and imported into the Bambu Studio slicer software for printing using a Bambu



Lab X-1 Carbon (Shenzhen, China) printer. Applicators were printed with 100% infill using FormFutura (Nijmegen, the Netherlands) Volcano PLA (FormFutura 2024). Shields were printed separately with 100% infill Rapid 3DShield (Stoughton, United States) tungsten filament (The Virtual Foundry 2024) and glued to their respective applicator using Clear Gorilla Glue (Cincinnati, United States). Figure 3 displays the printed applicators.

2.3. Experimental measurements

Measurements were performed in the Zeiss Intrabeam Water Phantom, using laser-cut Gafchromic EBT3 film held with a 3D printed film holder. The film holder, initially designed by Chin *et al* (2023), was modified to include rigid legs with a wider base instead of removable legs. The holder was 3D printed with 93% infill PLA using a Bambu Lab X-1 Carbon printer.



Figure 4. The experimental set-up of film irradiation. (a) The full set-up, with Zeiss Intrabeam Water Phantom and XRS visible. (b) The Zeiss Intrabeam Water Phantom. (c) Front view of the film irradiation set-up, with film holder holding film positioned against an applicator. (d) Side view of this set-up.

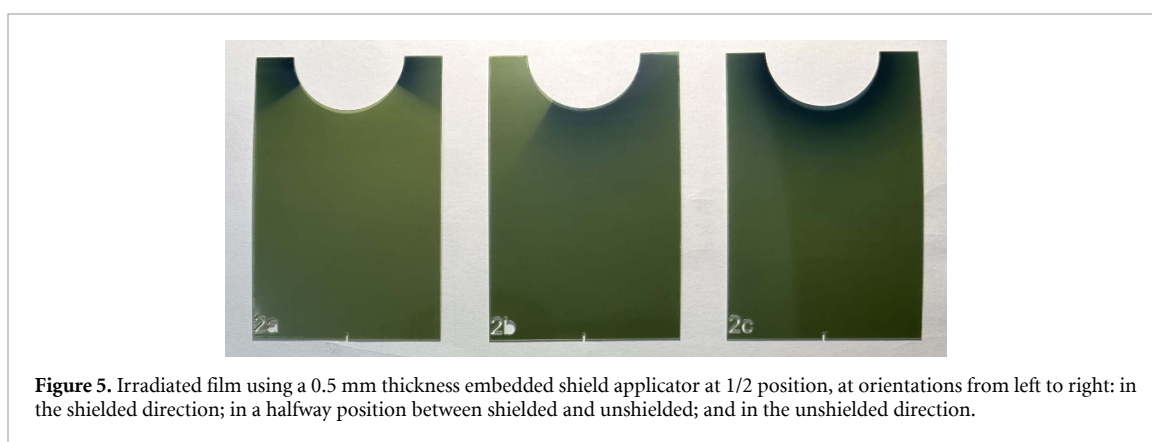


Figure 5. Irradiated film using a 0.5 mm thickness embedded shield applicator at 1/2 position, at orientations from left to right: in the shielded direction; in a halfway position between shielded and unshielded; and in the unshielded direction.

Film slices were designed on Autodesk Fusion360 and exported as *.dxf* files to Beam Studio, the software controlling the Flux Beambox laser cutter. The slices consisted of 90 mm \times 60 mm rectangles with a semi-circle or semi-ellipse cut into one edge, and Gafchromic EBT3 film was laser-cut to these designs.

The film was irradiated using a 50 kV energy setting, with a treatment prescription of 2 Gy at 10 mm from the applicator surface. Three films were stacked together in the film holder and submerged in the water tank. Due to the slow water penetration of Gafchromic film, dosimetric measurements in water are feasible (Devic *et al* 2010), and minimal water damage was observed. Figure 4 displays the experimental setup.

The film was pressed against the surface of the applicator, and care taken to ensure correct alignment. For each shielded spherical applicator, measurements were taken in three orientations: the shielded direction, the unshielded direction, and a direction halfway between. For the shielded ellipsoid applicator, measurements were recorded in both the shielded and unshielded directions, whilst measurements for the unshielded spherical and ellipsoid applicators were taken in only one orientation. Care was also taken to ensure no air bubbles were present. Following exposure, the films were immediately dried with paper towel and left to stabilise for approximately 20 h. Figure 5 shows examples of the irradiated films.

The film was scanned using an Epson 12 000 XL scanner, with a resolution of 300 dpi and 48-bit image type settings. Three scans were performed per film set. Using MATLAB R2024a, the red channel of each slice was extracted, as this channel is the most sensitive for film dosimetry at doses < 2 Gy (Papaconstadopoulos *et al* 2014). The film slices were registered together using the *imregister* function from the MATLAB Image Processing Toolbox, and an average image was generated. A 7×7 median filter was applied, and pixel values were extracted along the central *x*-axis. For spherical applicators, values were also taken along lines rotated by $\pm 5^\circ$ and averaged. For ellipsoid applicators, the central 11 rows were averaged. These values were then used to generate a PDD curve. The uncertainty for each pixel value was calculated using a combined standard deviation from both the averaged image and the average line.

When analysing the pixel values, relative comparison was employed since the response of film in the red channel at the specified energy (50 kV and below) is nearly stable (Villarreal-Barajas and Khan 2014), eliminating the need for calibration. Dose maps were generated from each averaged image, along with percentage difference maps comparing shielded and unshielded film directions.

3. Results

3.1. Dose maps

Normalised dose maps were generated for the central cross-sectional Z-plane of the applicators, using both MC simulations and film data. The plot axes represent the x- and y-distance from the applicator centre. Dose regions are displayed in 10% intervals, ranging from 0% to 100%, as indicated by the colour bar. Detailed MC dose maps are available in the [appendix](#), whilst figure 6 displays film dose maps compared to respective MC dose maps, with relative positions colour-coded.

3.2. PDD curves

MC PDDs were obtained along the x-axis in the shielded direction for each applicator model. All PDDs were normalised to the unshielded applicator's dose at a 2 mm distance from the applicator tip and plotted alongside the unshielded applicator. Applicators are grouped with other relevant applicators to enable comparison of shield variables. Errors are reported with a coverage factor of $k = 3$ (99.7%), with detailed descriptions of maximum error provided in the [appendix](#). The use of $k = 3$ is carried on from Chin *et al* (2023), and the high level of confidence is indicative of the high statistical precision of the data. All MC PDDs were fitted to curves using equation (2), with R^2 values provided in the [appendix](#). Figure 7 displays these PDD plots, each including an inset plot to better visualise the shielded applicator PDDs.

Similar PDD curves derived from film data are presented in figure 8. The unshielded applicator film data is plotted alongside each shielded applicator PDD, normalised to the unshielded applicator. Errors, calculated as the standard deviation of average pixel values, are often too small to be visually discernible. Table 4 lists the maximum film measurement uncertainty for each applicator as plotted in figure 8. Each plot in figure 8 also includes the MC data and its fitted curve for the respective applicators. A graph showing the differences between the fitted MC curves and the film data for both the unshielded and shielded applicator PDDs is displayed below each plot. The RMSE values comparing the fitted MC values to the film measurements are also provided in table 4.

3.3. Percentage difference of unshielded and shielded halves of applicator

Plots showing the absolute percentage difference between the unshielded and shielded halves of each applicator were obtained in the central cross-sectional Z-plane of the applicator, for both MC and film data. These mappings range from 0% to 100% in 10% intervals, as indicated by the colour bar. The plot axes represent the x- and y-distance from the applicator centre. Detailed MC percentage difference maps are available in the [appendix](#), whilst figure 9 displays film percentage difference maps compared to respective MC dose maps, with relative positions marked.

3.4. Energy spectra

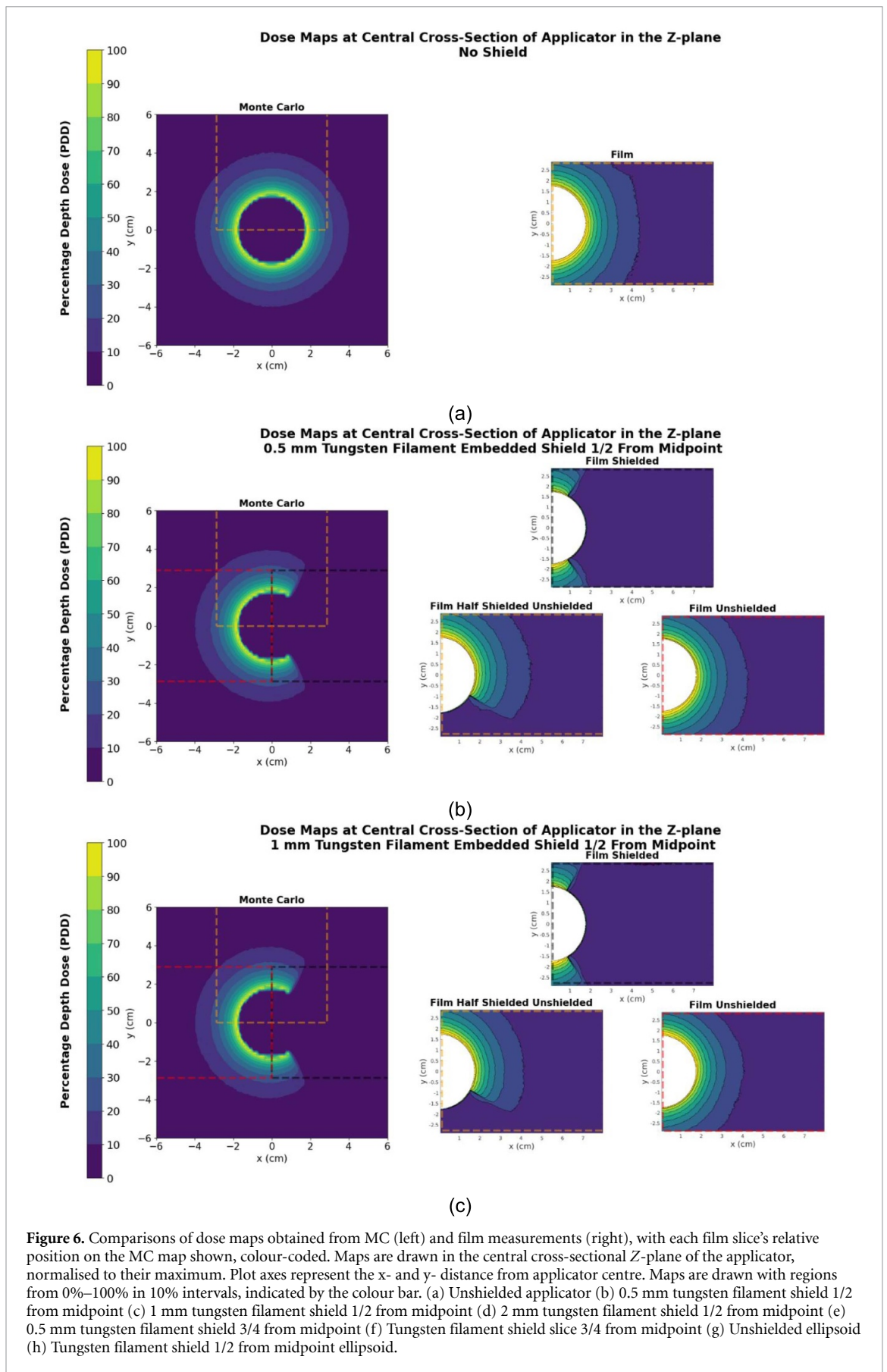
Energy spectra for each applicator, measured in the direction of the shield region, were obtained with MC data. Detailed spectra for all applicators are depicted in the [appendix](#), whereas spectra for relevant applicators are displayed in figure 10. All applicators are plotted on a single graph, with the mean photon energy of the shielded applicator indicated in the legend. The photon count is normalised to the maximum photon count of the unshielded spherical applicator.

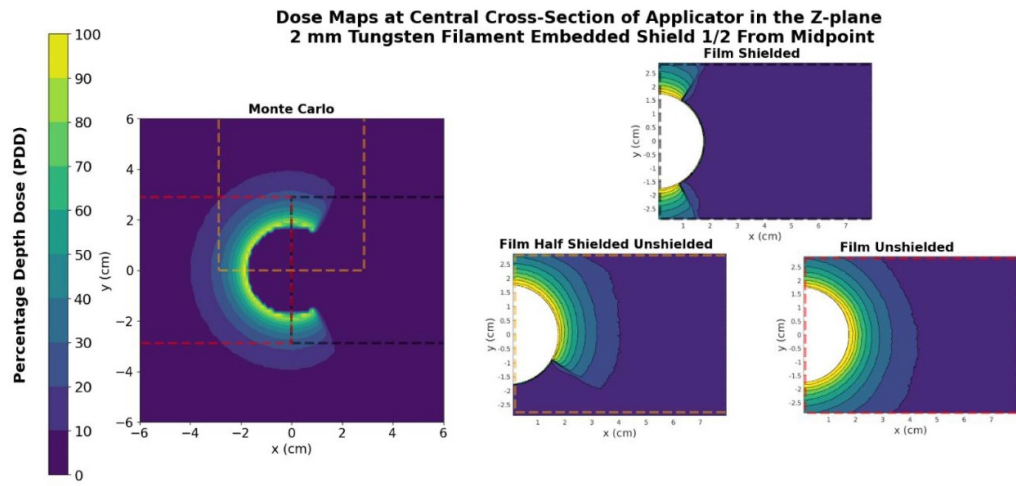
4. Discussion

4.1. Dose maps

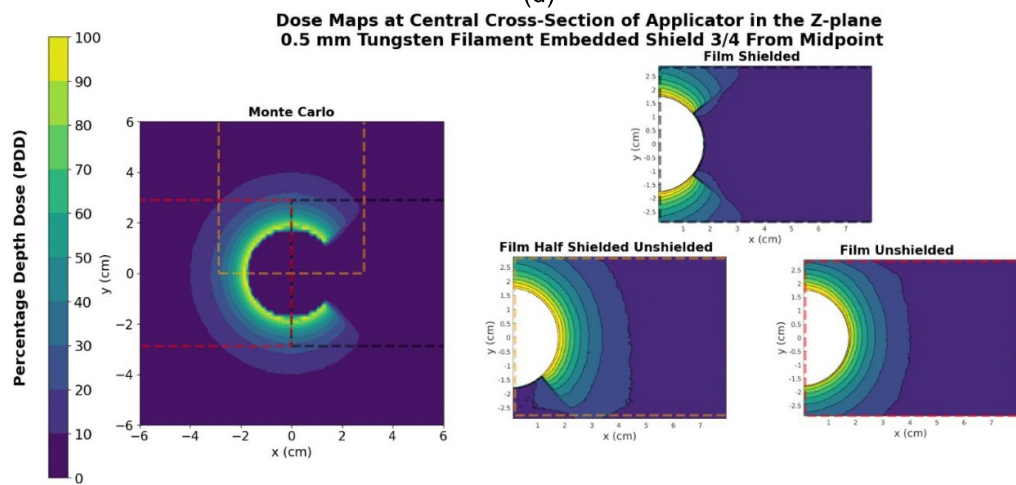
Figure 6 illustrates a comparison between film and MC dose maps, in the central cross-sectional Z-plane of the applicators, normalised to the maximum dose. Visual comparisons reveal close resemblances between the film and their corresponding MC maps. Both datasets exhibit the expected pattern of rapid isotropic dose fall-off, with shielded applicators displaying distinct regions of zero to low dose behind the shields. This pattern is consistently observed in both the film and MC maps. Slight differences between the film and MC maps are noted, particularly in minor outcrops at the edges of some film dose patterns, which are absent in the MC maps. These outcrops may result from minor positioning errors of the film or applicator, or may reflect the film's sensitivity, as similar patterns are observed in the log dose maps in the [appendix](#). Another discrepancy is evident in figure 6(g), where the 10%–20% dose region appears to extend 1–2 cm further in the film map compared to the MC map. However, this anomaly is absent in the unshielded region in figure 6(h), suggesting a minor error in either the film or scanning process. Overall, however, the high correlation between the MC and film data provides confirmation of the validity of the MC simulations.

In comparing the shield variables, increasing the thickness of the embedded shields beyond 0.5 mm has less than 0.3% effect on the distribution, suggesting that thicker shields offer no additional benefit and

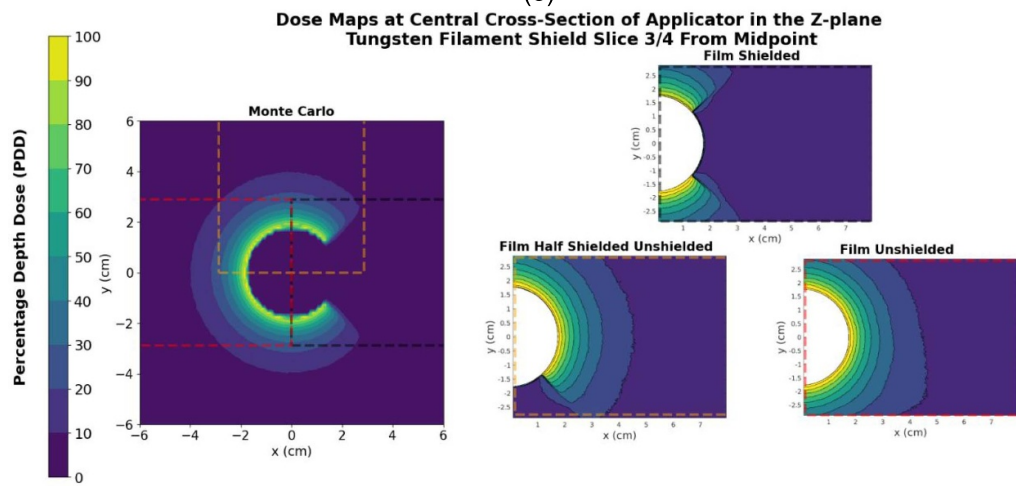




(d)

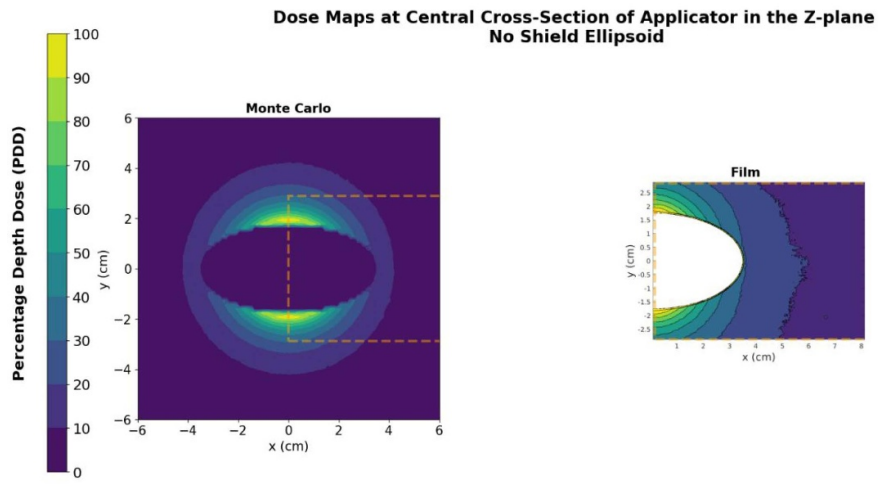


(e)

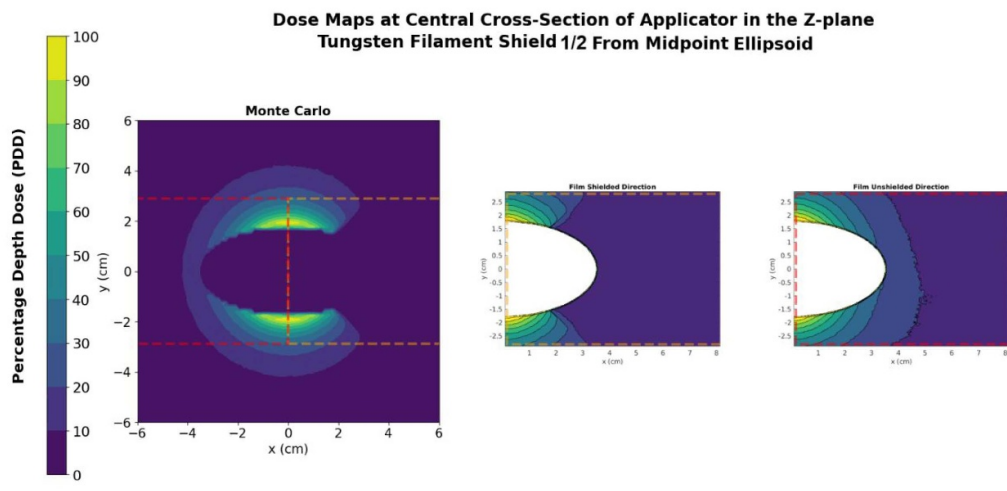


(f)

Figure 6. (Continued.)



(g)



(h)

Figure 6. (Continued.)

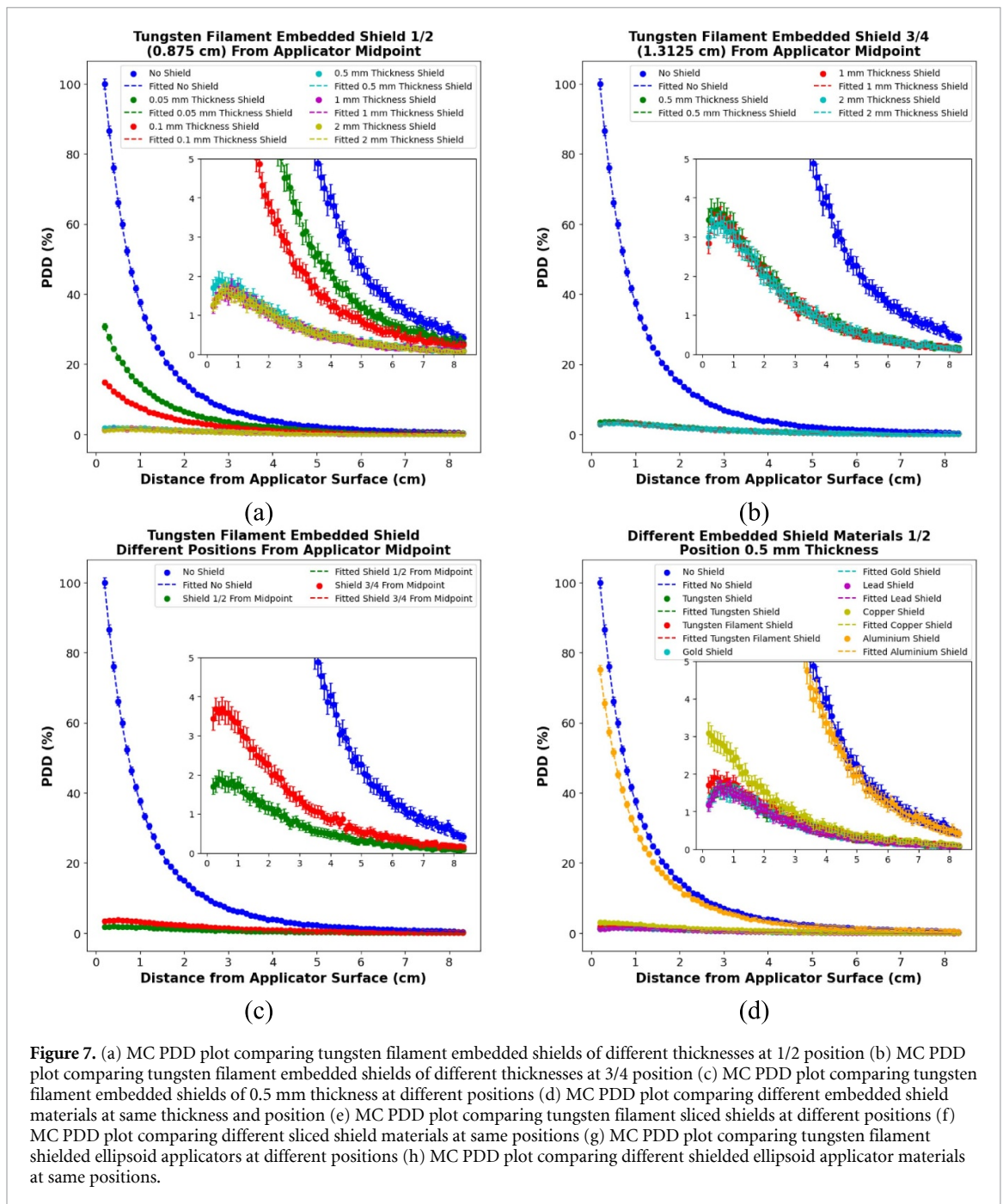


Figure 7. (a) MC PDD plot comparing tungsten filament embedded shields of different thicknesses at 1/2 position (b) MC PDD plot comparing tungsten filament embedded shields of different thicknesses at 3/4 position (c) MC PDD plot comparing tungsten filament embedded shields of 0.5 mm thickness at different positions (d) MC PDD plot comparing different embedded shield materials at same thickness and position (e) MC PDD plot comparing tungsten filament sliced shields at different positions (f) MC PDD plot comparing different sliced shield materials at same positions (g) MC PDD plot comparing tungsten filament shielded ellipsoid applicators at different positions (h) MC PDD plot comparing different shielded ellipsoid applicator materials at same positions.

increase material costs. In terms of shield positioning, moving the embedded shield further from the midpoint tightens the gap in the distribution behind the shield. When comparing the sliced and embedded shields in similar positions (figures 6(e) and (f)), both produce nearly identical dose maps, indicating that the shield type has minimal impact on the resulting distribution. Since sliced shields require more material, embedded shields are likely the more practical and cost-effective option. The unshielded ellipsoid applicator produces a dose map visually similar to the spherical applicator, except for the regions of no dose where the ellipsoid exists. The ellipsoid applicator can dampen dose in specific areas while maintaining high doses in others. Its shape may also displace tissue away from high-dose regions, offering potential advantages in certain clinical scenarios. Based on the film data shown in figure 8(f), the shielded ellipsoid applicator achieves dose reductions of about 99%, 48%, 22%, and 8% at 0.3 cm, 1 cm, 2 cm, and 3 cm from the applicator surface, respectively. Combining the ellipsoid shape with shielding could facilitate more complex dose distributions and treatment plans.

The dose maps provide valuable data for characterising each applicator, laying the groundwork for future research or clinical applications. This data can be compared to the distributions required for clinical use, enabling treatment planning for patient-specific mIORT. By matching planned distributions to those

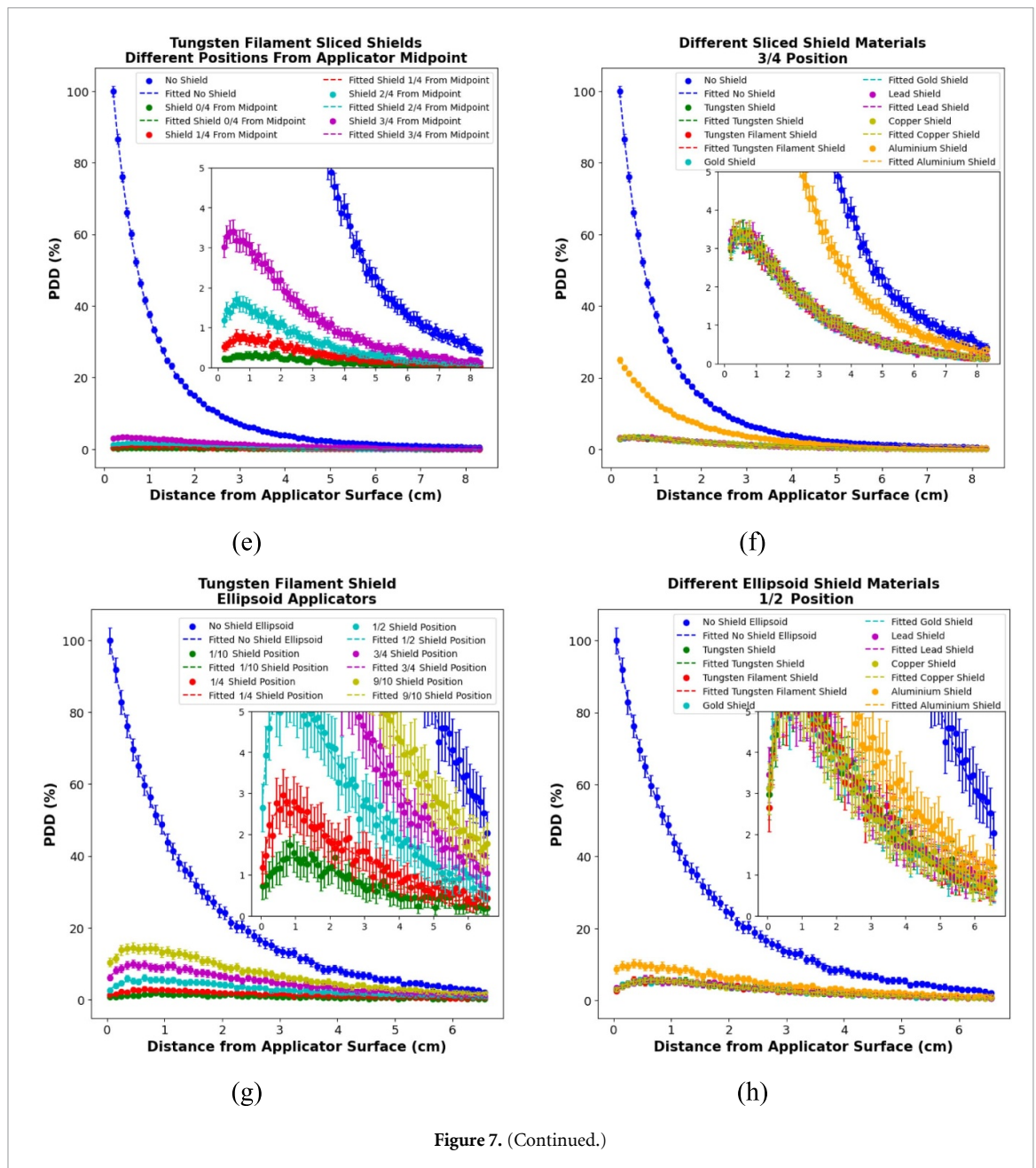


Figure 7. (Continued.)

generated in this study, specific applicators can be designed and used in treatments, enhancing the precision and efficacy of therapeutic interventions.

4.2. PDD curves

Figure 7 displays PDD plots of multiple applicators obtained from MC, along with fitted curves. The PDDs are generated in the x -axis shielded direction, with multiple applicators plotted together on the same axis, normalized to the maximum of the unshielded applicator. Relevant applicators are grouped to enable comparisons between shield variables. Regarding MC errors along this axis, most maximum errors are below 1%. The highest error is 3.6% for the unshielded ellipsoid, followed by 1.5% for the unshielded spherical applicator. As the errors are relatively low, the results demonstrate a high degree of statistical precision and reliability. The R^2 values for all fitted curves are close to 1, with the lowest being 0.9291, indicating strong fits.

Figure 7(a) shows the effect of varying the embedded shield thickness for the tungsten filament material at 1/2 position from the midpoint. From the inset plot, it is evident that both 1 mm and 2 mm thickness shields produce nearly identical PDD curves, whereas the 0.5 mm thickness results in PDDs that begin with about 0.3% higher doses before levelling out. A similar trend, though less pronounced, is indicated in figure 7(b), with 3/4 position from the midpoint. These results are consistent with the dose maps, apart from the 0.5 mm thickness, although its difference compared to the 1 mm and 2 mm thickness is only minor.

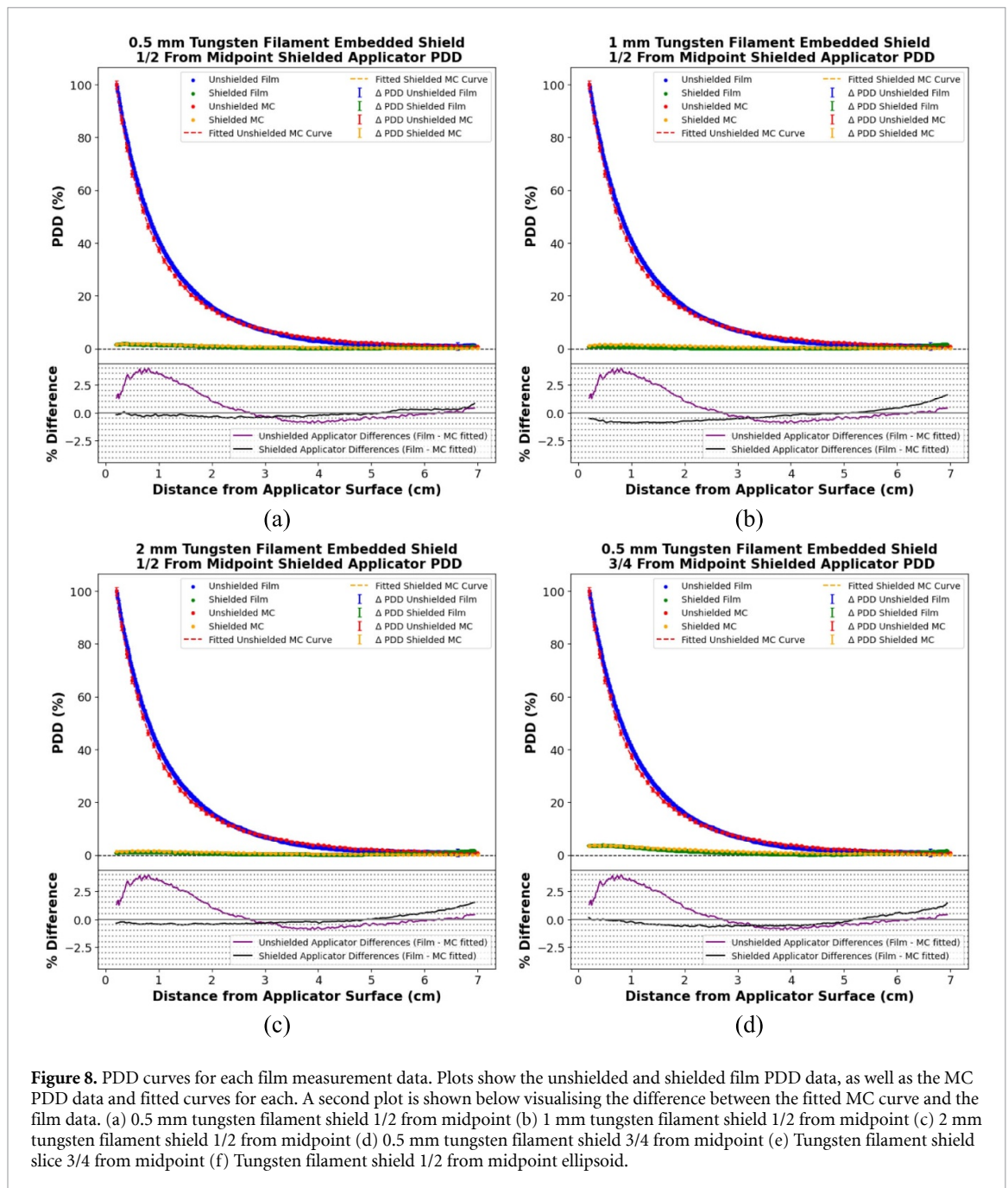


Figure 8. PDD curves for each film measurement data. Plots show the unshielded and shielded film PDD data, as well as the MC PDD data and fitted curves for each. A second plot is shown below visualising the difference between the fitted MC curve and the film data. (a) 0.5 mm tungsten filament shield 1/2 from midpoint (b) 1 mm tungsten filament shield 1/2 from midpoint (c) 2 mm tungsten filament shield 1/2 from midpoint (d) 0.5 mm tungsten filament shield 3/4 from midpoint (e) Tungsten filament shield slice 3/4 from midpoint (f) Tungsten filament shield 1/2 from midpoint ellipsoid.

Hence, it can be concluded that shields thicker than 0.5 mm provide limited additional benefit. Figure 7(c) indicates the effects of the embedded shield's position, using a 0.5 mm thickness. The 3/4 position shield, despite having the same thickness, produces a PDD with a higher dose than the 1/2 position shield. This is likely due to scatter from the unshielded sections in the 3/4 position that are shielded in the 1/2 position. Hence, the dose behind embedded shields of the same thickness increases as the position moves further from the applicator midpoint. Figure 7(d) compares the effect of shield material at 1/2 position with a 0.5 mm thickness. Clearly, aluminium produces a PDD less than 1% lower than the unshielded applicator, whereas other materials exhibit low and relatively similar PDDs. The inset plot shows that copper provides a higher dose than the other materials before levelling out. Tungsten filament produces about 0.2% higher dose than pure tungsten, gold and lead; however, the difference is marginal. Considering tungsten filament's ease of use in printing shields, it is likely the most practical material. Figure 7(e) presents the effect of shield position for the sliced shields. As the shield's position moves further from the midpoint, the PDD curves increase, as expected, due to reduced thickness and increased scatter from unshielded regions. Comparing this plot with figure 7(c), specifically the 1/2 and 3/4 positions, the sliced shields produced PDDs about 0.3% lower than the embedded shields in similar positions. Although dose maps suggest that that embedded and sliced shields at the same positions yield similar results, the PDDs indicate a slight difference. Thus, if additional shielding

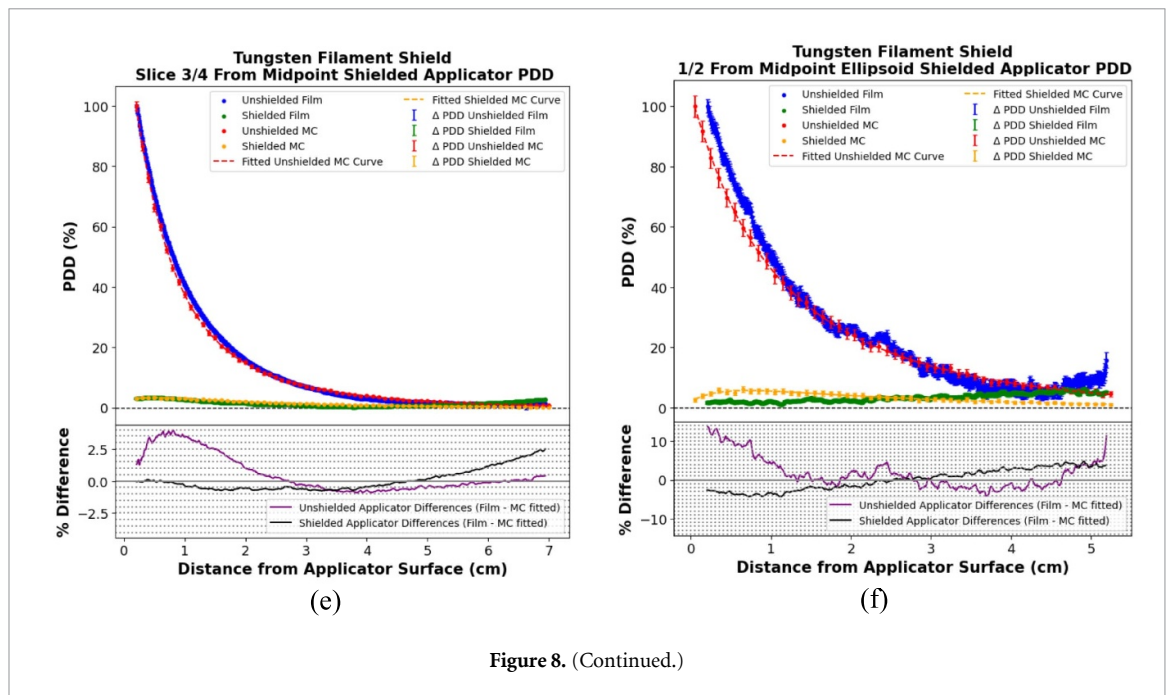


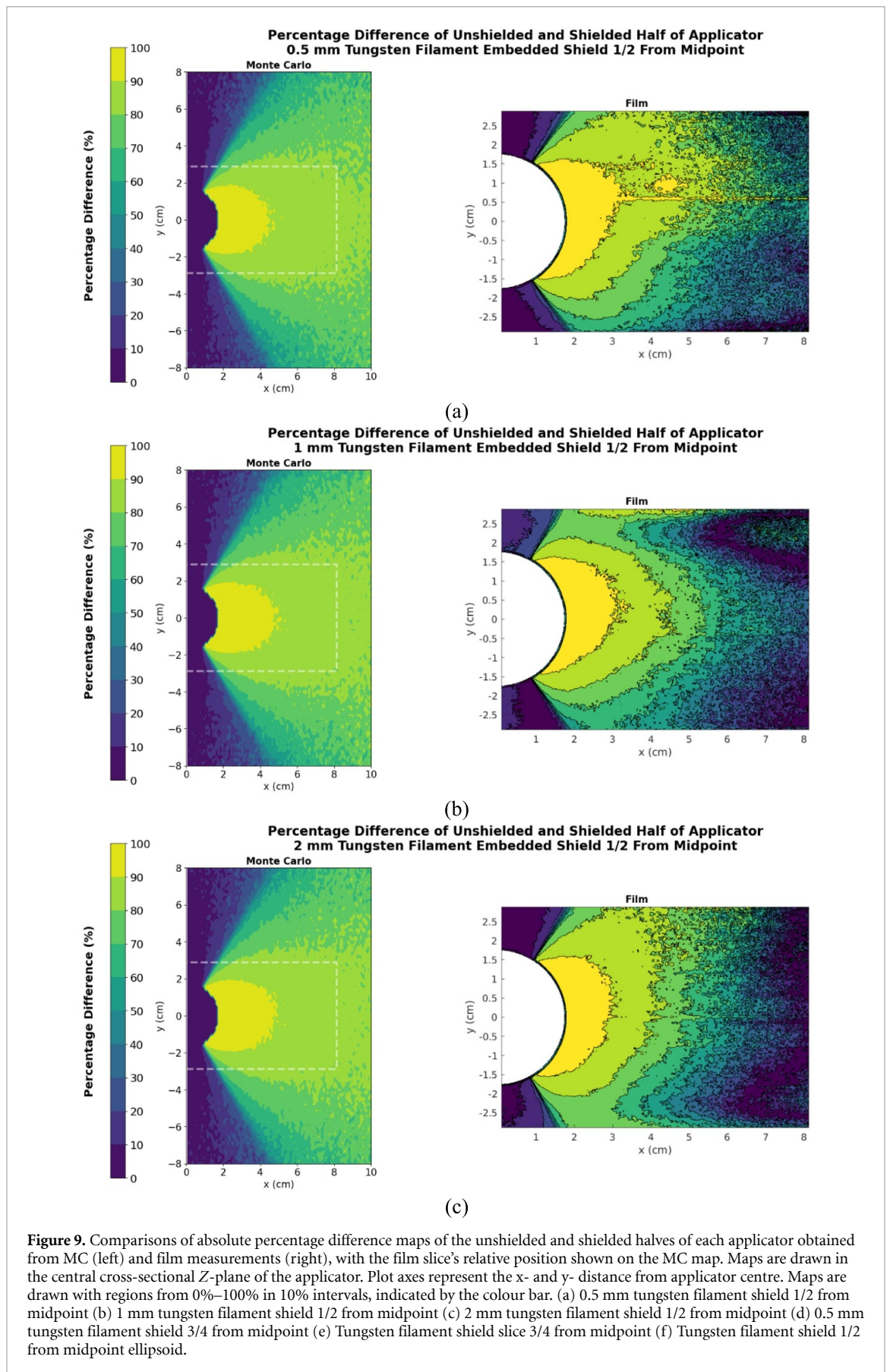
Figure 8. (Continued.)

Table 4. Maximum film uncertainty for each applicator, along with the RMSE of each fitted MC curve to the film values.

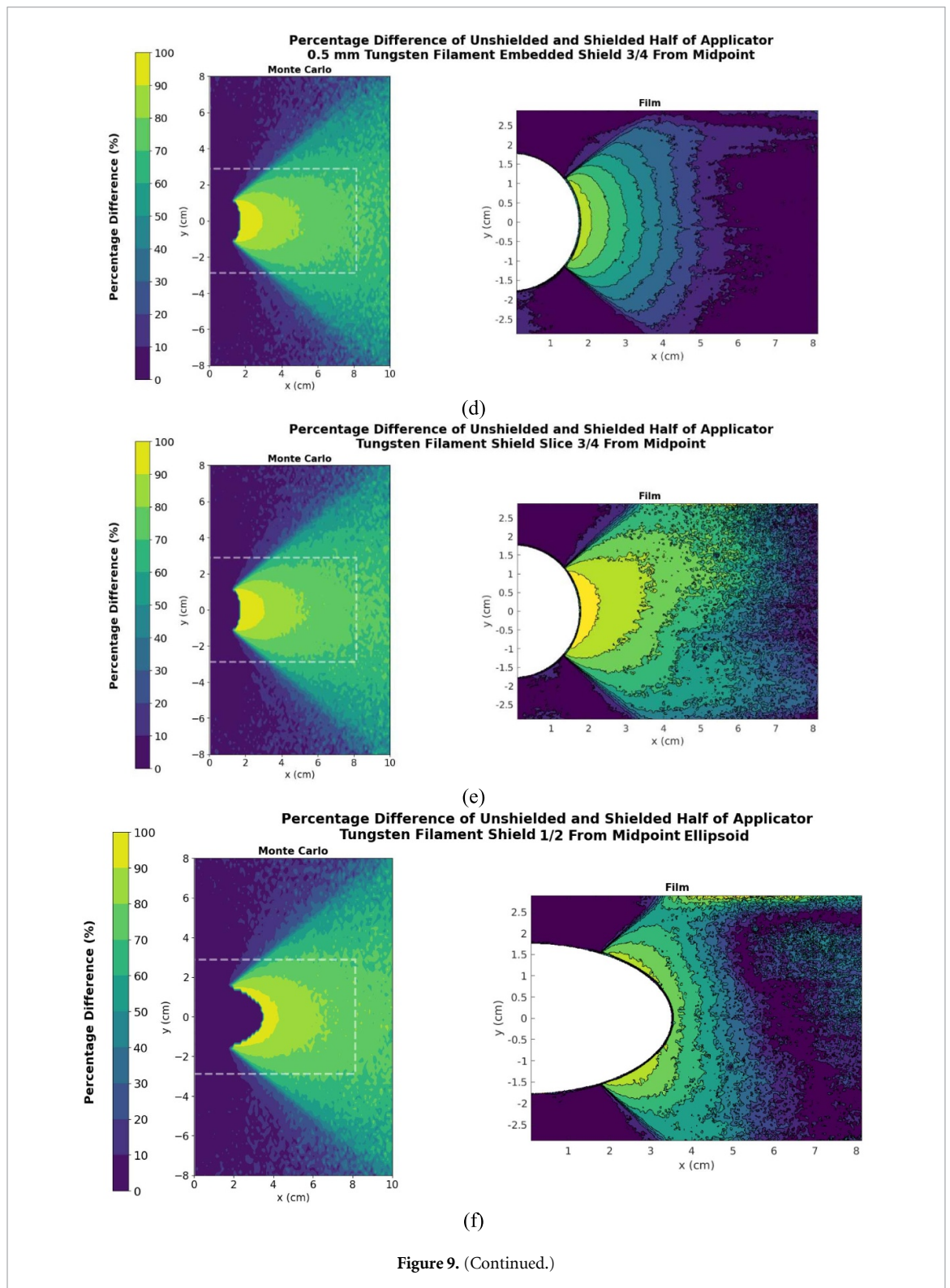
Applicator	Maximum film uncertainty (%)	RMSE
No shield	3.9	0.05
0.5 mm tungsten filament embedded shield 1/2 from midpoint	3.8	0.01
1 mm tungsten filament embedded shield 1/2 from midpoint	3.1	0.02
2 mm tungsten filament embedded shield 1/2 from midpoint	4.3	0.02
0.5 mm tungsten filament embedded shield 3/4 from midpoint	3.4	0.02
Tungsten filament shield slice 3/4 from midpoint	1.6	0.03
No shield ellipsoid	2.3	0.18
Tungsten filament shield 1/2 from midpoint ellipsoid	3.0	0.11

is required for similar dose distributions, sliced shields may be employed instead of embedded shields. Figure 7(f) indicates, like figure 7(d), that shield material has minimal impact on the sliced shield PDD, apart from aluminium. Figure 7(g) illustrates ellipsoid PDDs with shields at different positions from the midpoint, showing similar patterns to figure 7(e), where positions further from the applicator midpoint leads to higher PDDs. Similar conclusions regarding shield material effects discussed previously can be drawn from figure 7(h).

Figure 8 presents PDD plots taken from film measurements, plotted alongside corresponding MC PDD and fitted curves. Each applicator is plotted alongside the unshielded applicator and normalised to the unshielded applicator's maximum dose. A sub-plot below each graph highlights the difference between the fitted MC curve and the film PDD curve. Table 4 lists the maximum uncertainty in film measurements for each film PDD, along with the RMSE between each fitted MC curve and film data. All maximum errors are below 4.5%. The relatively low film uncertainties indicate the high precision of the film measurements, reflecting the reliability of the data. Regarding differences between the MC and film data, the secondary plots show deviations below 4% for the unshielded spherical applicator, and below approximately 3% for shielded spherical applicators. These relatively low differences are also reflected in their RMSE values, which for all spherical applicators are below 0.03, demonstrating a high degree of agreement between the MC and film data. For the ellipsoid applicators, however, the maximum deviation between MC and film data for the unshielded applicator is around 14%, whilst for the shielded applicator, it is 5%. This is also reflected in the RMSE values, which are higher for ellipsoids compared to spherical applicators, each exceeding 0.11. Visually, the film data does not align as closely with the MC data for ellipsoid applicators as it does for spherical applicators. The higher differences are likely due to the low signal in regions farther from the applicator's midpoint, where noise is more prevalent. It is expected that increasing the dose prescription to enhance the signal would yield comparable results to those seen with spherical applicators. Nevertheless, the relatively low RMSE values for each ellipsoid applicator indicate a high correspondence between the MC and film data, validating the MC simulations.



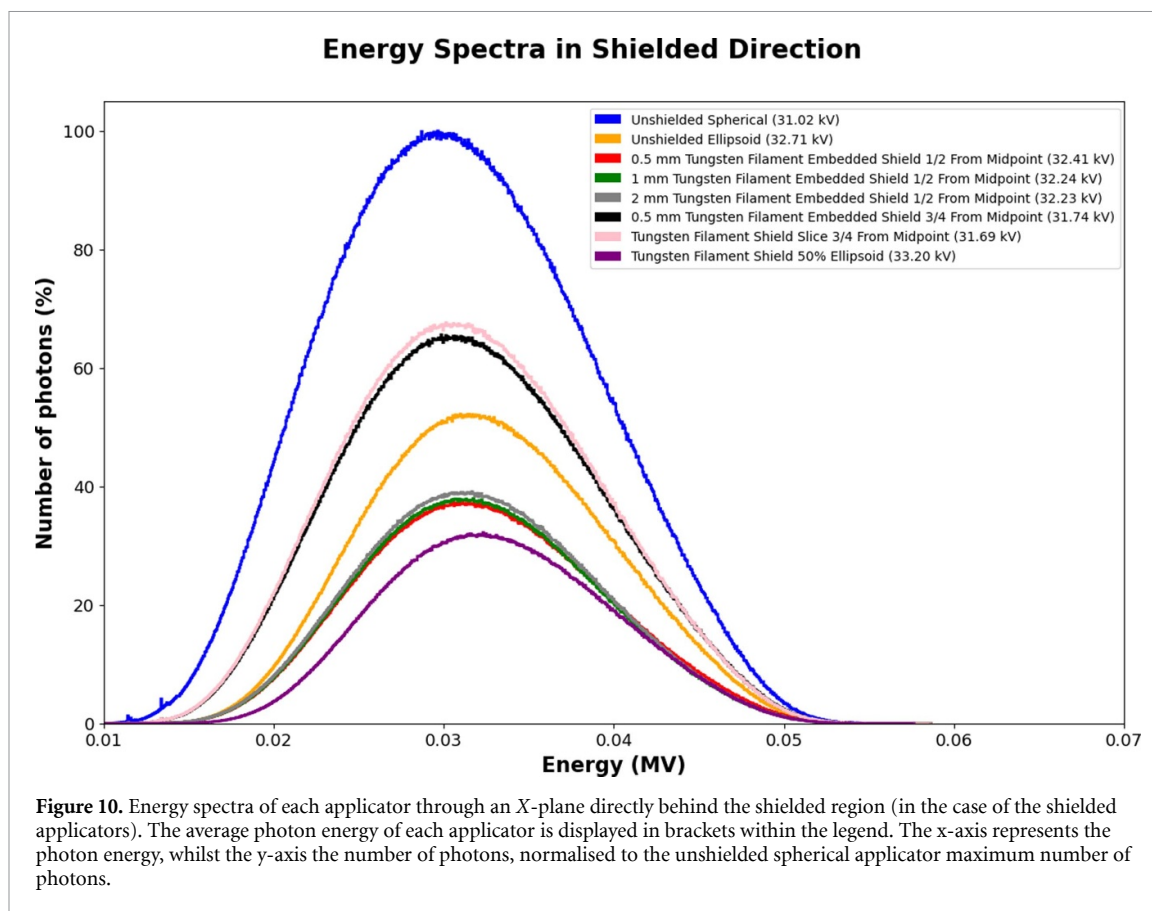
All plots provided here give further means of characterising the shielded applicators for potential future practical use. By determining the PDDs for different applicators, the dose delivered behind each shield can be quantified, offering insights into potential dose delivered to critical regions shielded by the applicator.



Therefore, applicators can be chosen for patient-specific IORT based on their dose delivery to these regions.

4.3. Percentage difference of unshielded and shielded halves of applicator

Figure 9 shows plots of the absolute percentage difference between the unshielded and shielded halves of each applicator for both MC and film data. The films' relative position on the MC map are marked. The plots indicate the effectiveness of each shield and their spatial effects on the dose distribution of each applicator. A higher percentage difference indicates superior shielding, with the highest differences in each plot occurring directly behind the shield. These plots, therefore, emphasize the effects of shielding, and the spatial patterns



produced. In terms of comparisons between shield variables, the same conclusions outlined previously can be drawn.

When comparing the film and MC maps, whilst the patterns produced by the film resemble those of the MC maps, the percentage difference falls off too quickly in the film compared to the respective MC. This discrepancy arises from the lack of signal in the film at increased distances from the applicator. Therefore, the signal drops to near zero more quickly for both halves, leading to this pattern. If a higher dose were prescribed, more signal would be available in the outer regions, leading to maps resembling the MC patterns. However, the overall similarity in patterns offers some support for the validity of the MC simulations, although not as strongly as the dose maps or PDD curves discussed earlier.

These plots provide another method for characterising the different applicators by indicating the effect of shielding on the region behind the shields and hence offering insight into the dose delivered to potentially critical regions.

4.4. Energy spectra

Figure 10 displays energy spectra of each relevant applicator, taken in the direction of the shielded region, and obtained using MC data. The mean photon energy of each applicator is displayed in the legend.

The spectrum for each shield demonstrates a trend of greater attenuation with increasing shield thickness, as evident from the peaks of their spectra compared to the unshielded applicator and one another. Shields positioned closer to the applicator midpoint result in greater attenuation. Ellipsoid applicators exhibit greater attenuation compared to spherical due to the increased physical distances from the applicator surface. Comparing the mean photon energies of shielded applicators to the unshielded, the shielded applicators exhibit higher mean energies than the unshielded. This is the effect of beam hardening, where a greater proportion of low-energy photons are attenuated by the shield compared to high-energy photons. Consequently, the peak of the spectra shifts toward higher energies, resulting in an increase in the mean energy. All energies reported here are consistent with the use of a 50 kV Intrabeam source. The energy spectra and mean energies of each of these applicators provide a final method for characterising each applicator, offering insights into the effects of shielding on photon attenuation and energy distribution. These findings could be applied in future work on developing a treatment planning system for patient-specific IORT.

These novel applicators hold significant potential for advancing IORT by providing tailored dose modulation capabilities. For instance, in breast cancer surgeries, the ellipsoid applicator's ability to shape the dose distribution could be particularly advantageous in sparing sensitive organs. The main organs at risk include the skin, chest wall, lung and heart (Grimm *et al* 2024). IORT has been used in brain metastases or head-and-neck tumours (Kyrgias *et al* 2016) and locally recurrent rectal cancer (Calvo *et al* 2020). The shielded designs could enable precise dose delivery to irregularly shaped tumour beds while minimizing exposure to sensitive organs. Such adaptability is a key improvement over conventional IORT applicators, which often lack this level of customization, making these modifications particularly valuable for complex clinical scenarios such as in the head and neck tumours close to salivary glands or spinal cord, to prevent radiation induced xerostomia or myelopathy.

The ability to customize dose modulation with these applicators introduces opportunities to improve the therapeutic ratio in challenging cases. For instance, in paediatric treatments of sarcomas or other solid tumours (Conte *et al* 2024), where minimizing radiation exposure to healthy tissue is critical, these applicators could enable safer treatments. The modularity of the designs allows for rapid adaptation to different tumour geometries, potentially expanding the scope of IORT to more diverse clinical contexts.

The application of these applicators is not limited to tumours close to critical organs, as IORT has been used for treatment of cases such as of extremity soft tissue sarcomas with incomplete resections. The aim is to preserve the limb with acceptable local control (Pilar *et al* 2017). Shielded applicators can still reduce dose to nearby organs in line with the ALARA principle although they may not be critical organs.

5. Conclusion

This study investigated the incorporation of novel applicators into the existing Zeiss IORT system to enable dose modulation, and characterised these applicators through dosimetric evaluation. EGSnrc MC simulations were performed to evaluate the dose distribution of each applicator, and these simulations were verified through film dosimetry in a water phantom. The data generated in this study can be used for the future development of patient-specific mIORT techniques, whereby specific applicator designs tailored to their characterised dose distributions are matched to treatment-specific requirements. This approach will lead to enhanced dose conformity to the tumour bed during IORT and, consequently, an improved therapeutic ratio. Future studies could explore additional applicator designs, the use of polyetherimide instead of Volcano PLA in 3D printing the applicators, or the development of a treatment planning system incorporating mIORT.

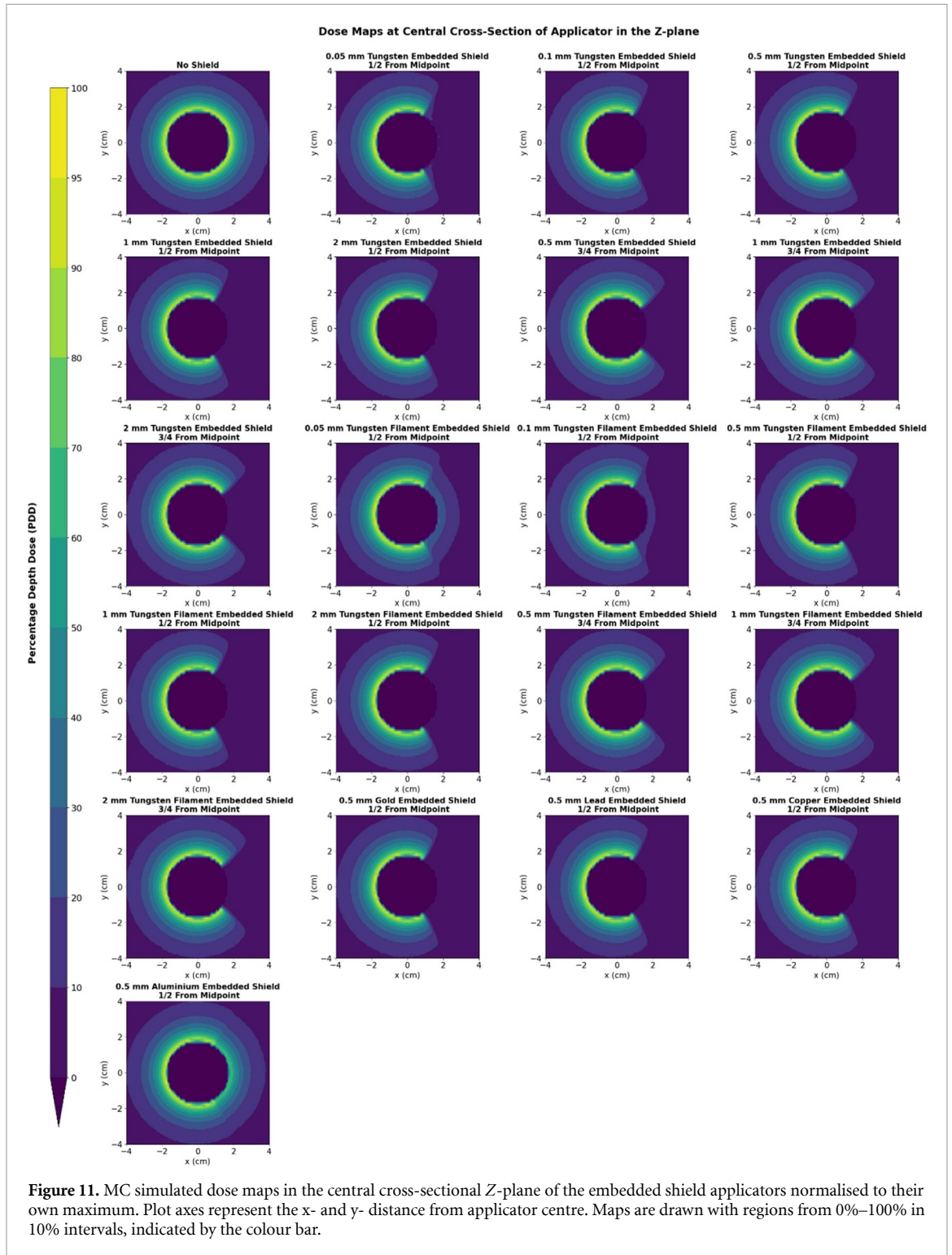
Data availability statement

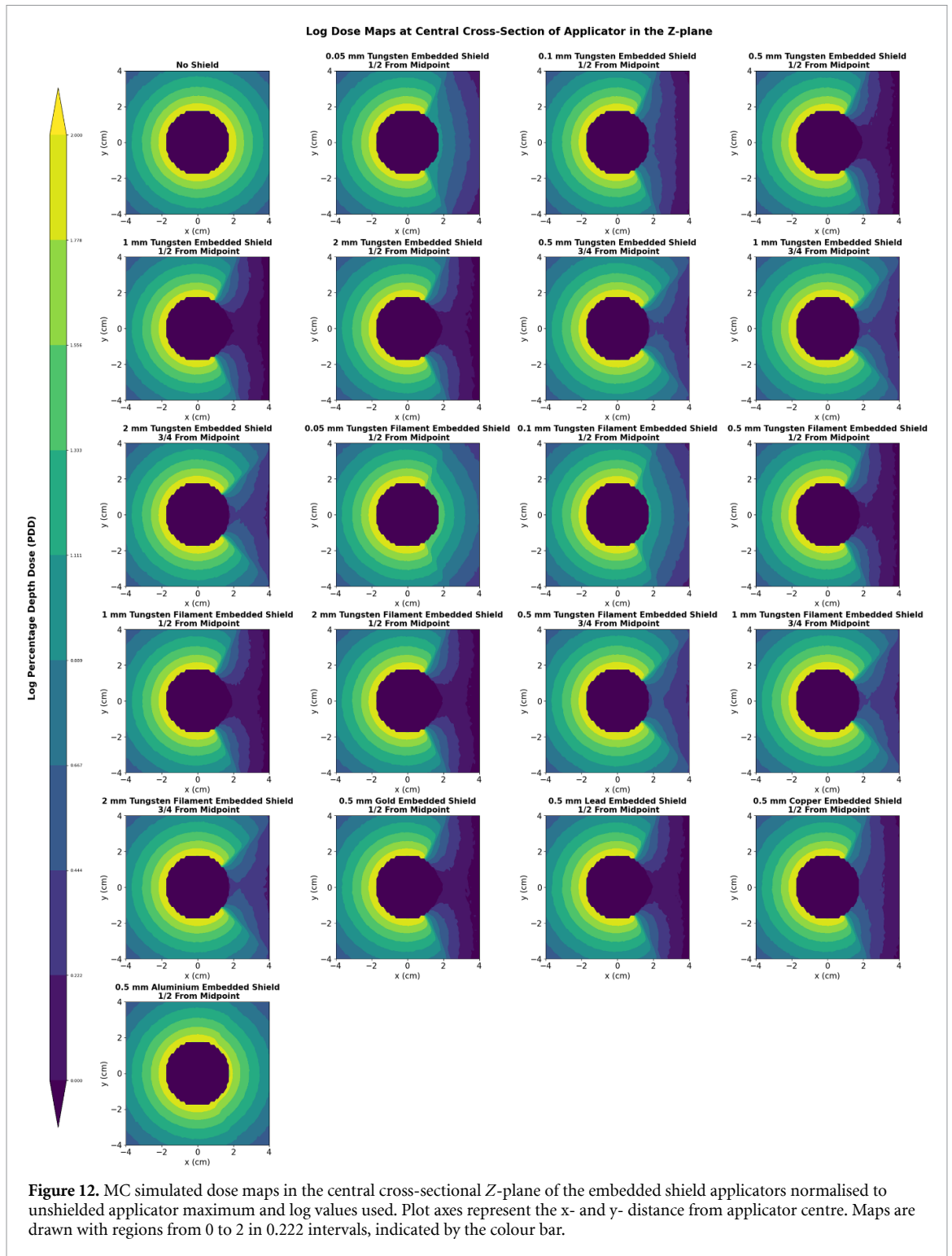
All data that support the findings of this study are included within the article (and any supplementary information files).

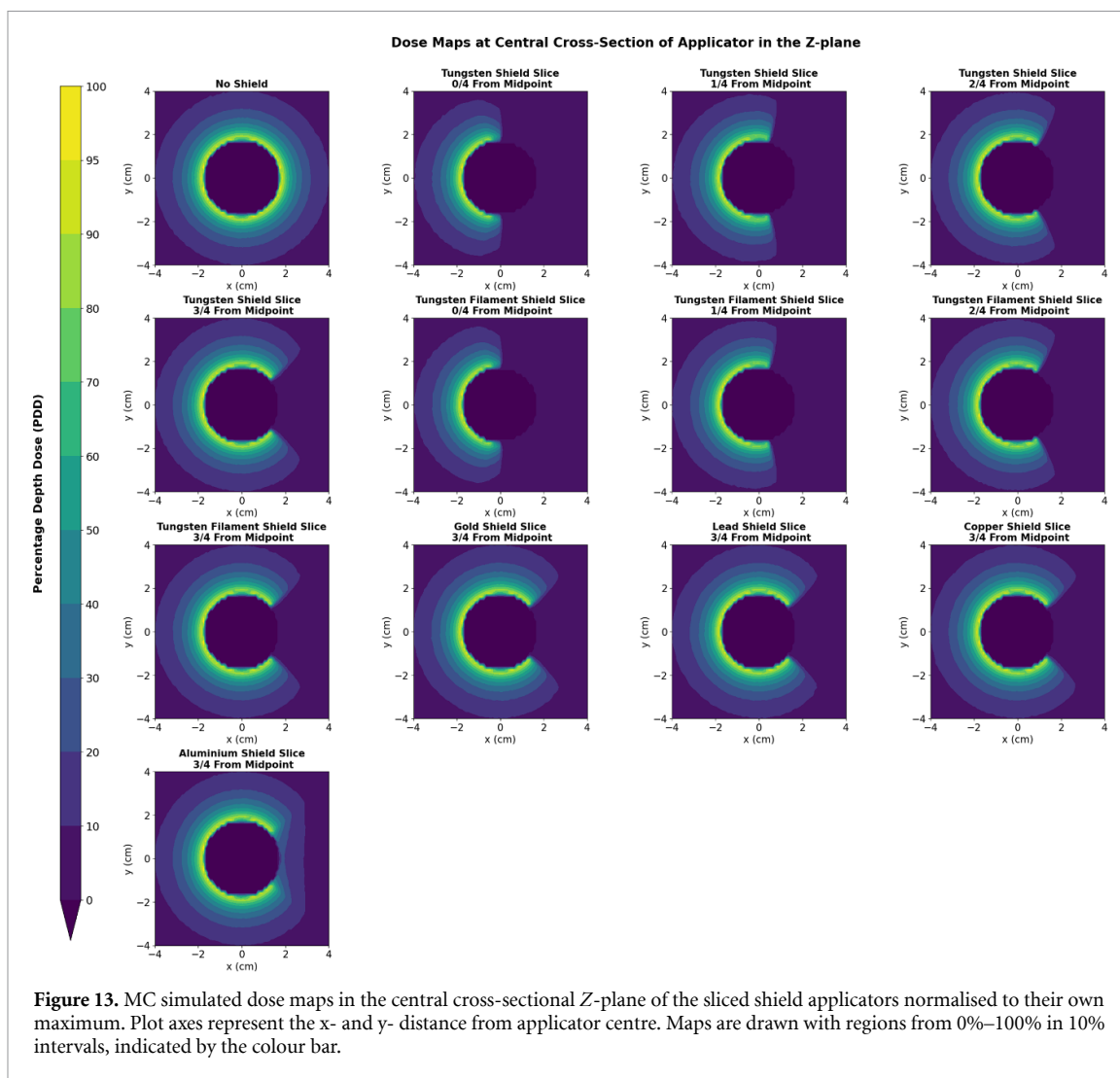
Acknowledgment

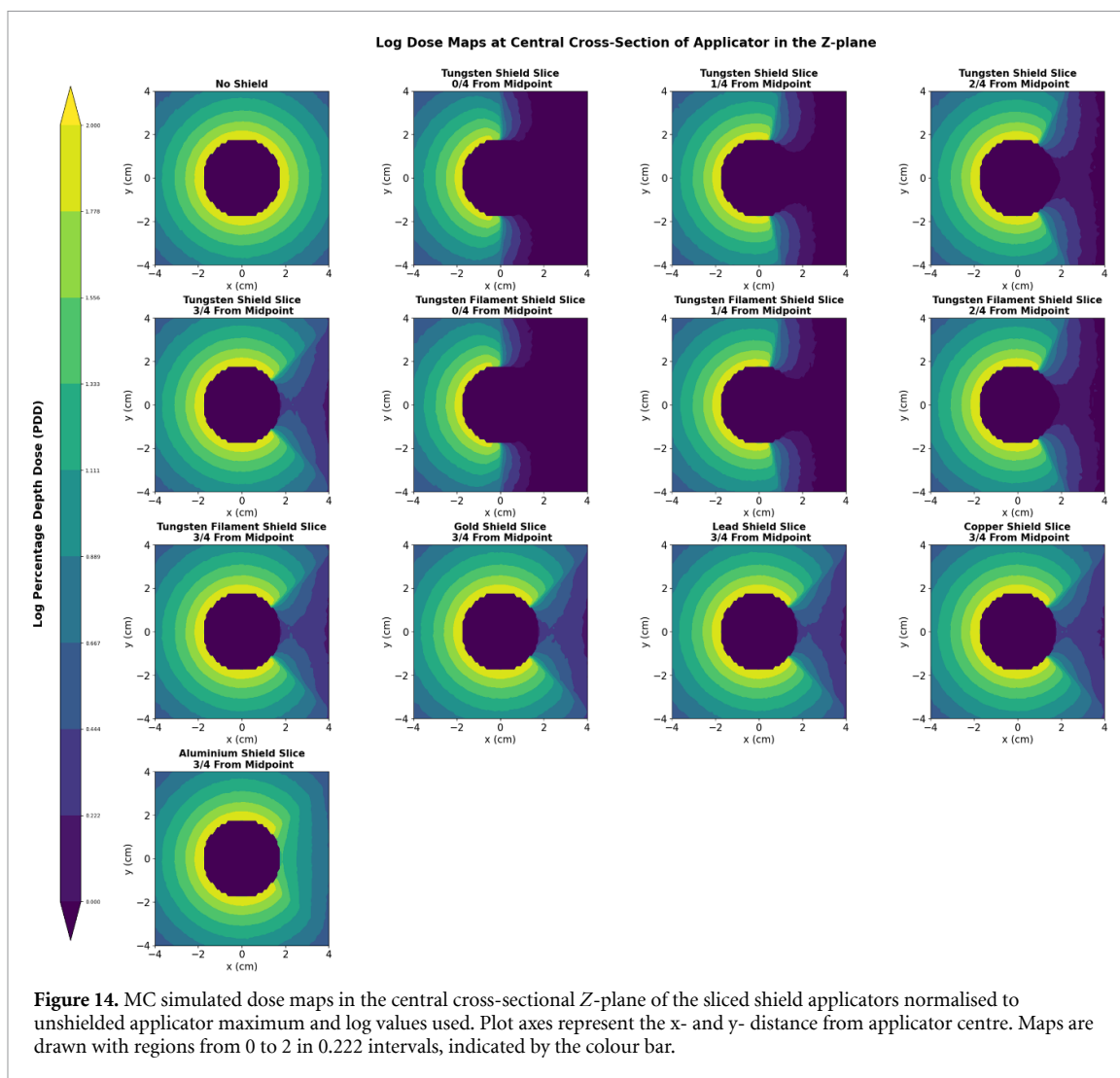
This work was partly supported by the WA Department of Health Merit Award. Special thanks to the Department of Radiation Oncology at Sir Charles Gairdner Hospital (Perth, Western Australia) for funding this research and providing the equipment. A thank you to Gavin Pikes and James Harris for their assistance in configuring a PC for use in MC simulations and setting up ssh tunnelling on it respectively. Also, a thank you to Kaylee Molin for her help in film scanning. An appreciation to Mahsheed Sabet for assisting me in acquiring X-rays of applicators previously taken by Chin *et al*. We acknowledge Reid Townson from the National Research Council Canada for his assistance and responses to questions regarding EGSnrc on an online forum. Appreciation to Ashlesha Gill and Andrew Hirst in their assistance in choosing a suitable filament for applicator 3D printing. A final thank you to Mahsheed Sabet for her help in responding to the reviewer's comments.

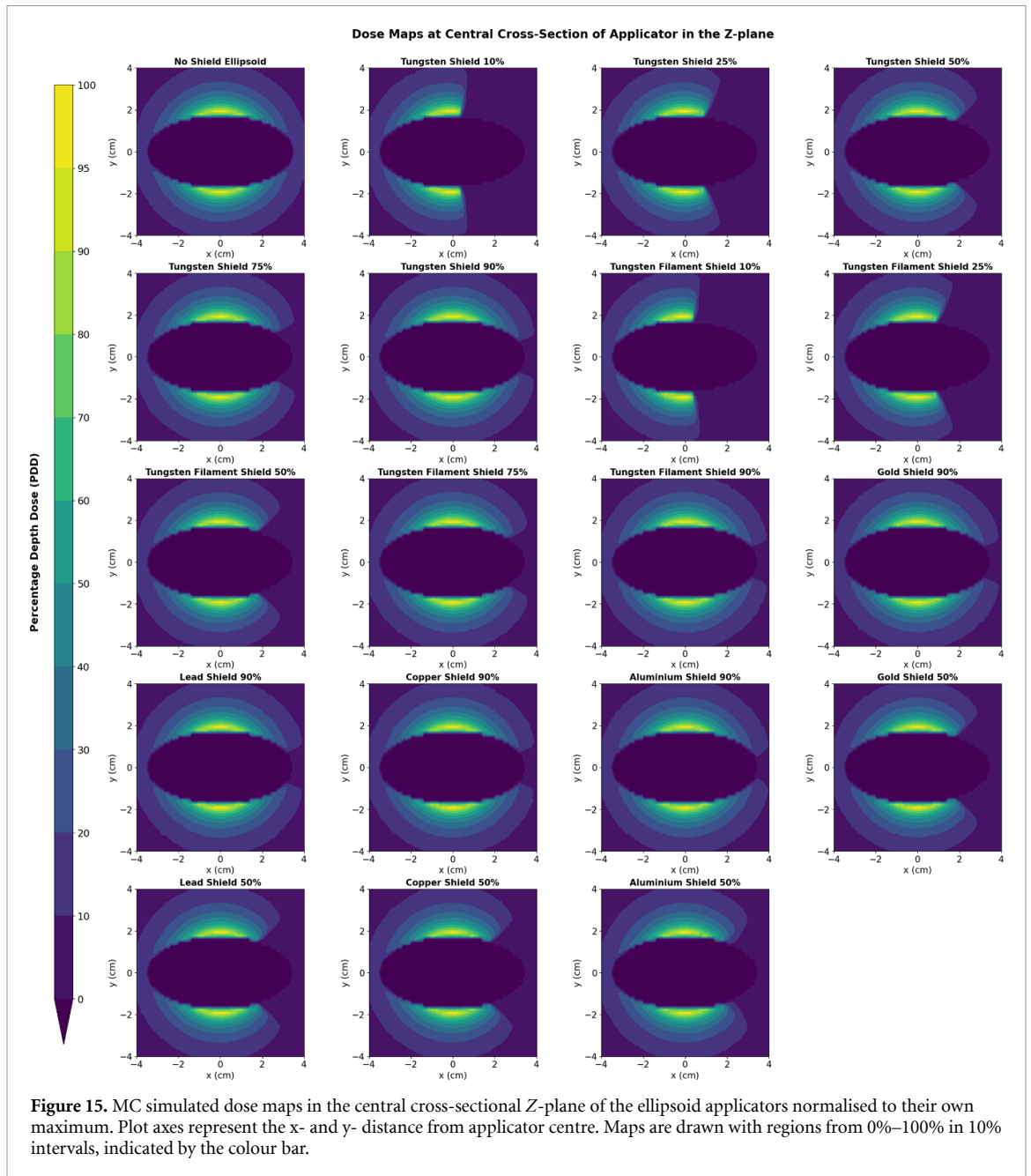
Appendix











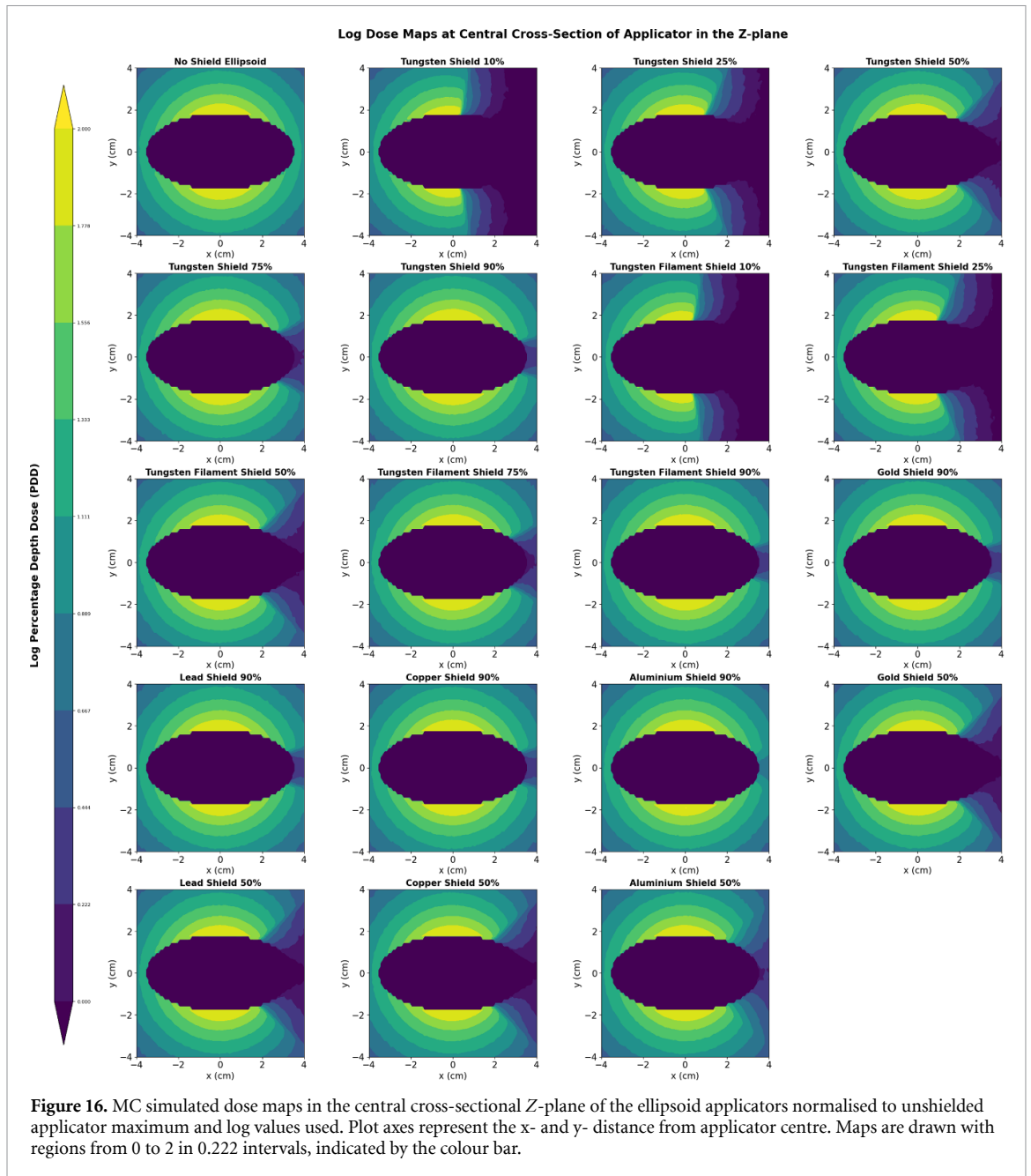
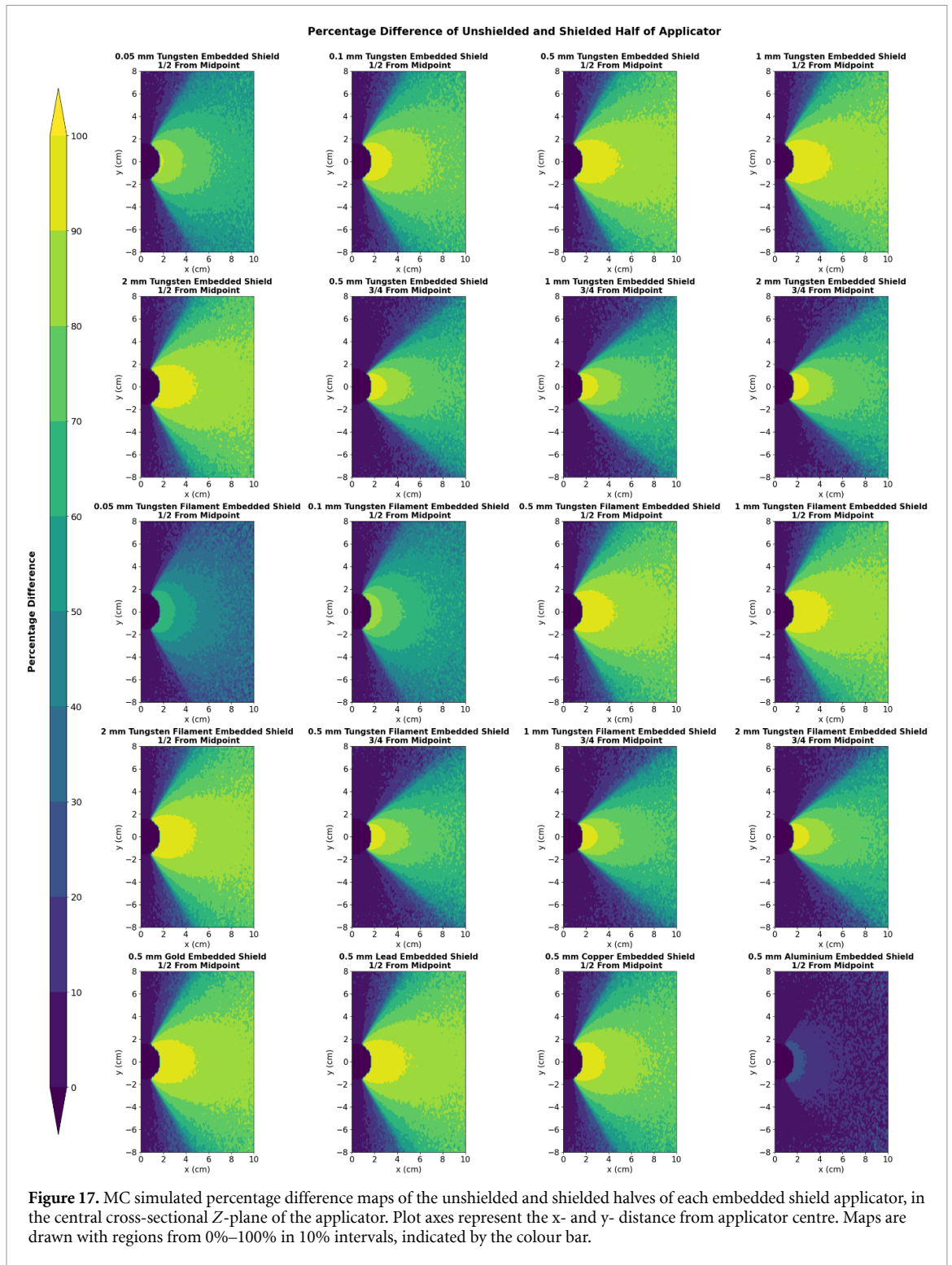
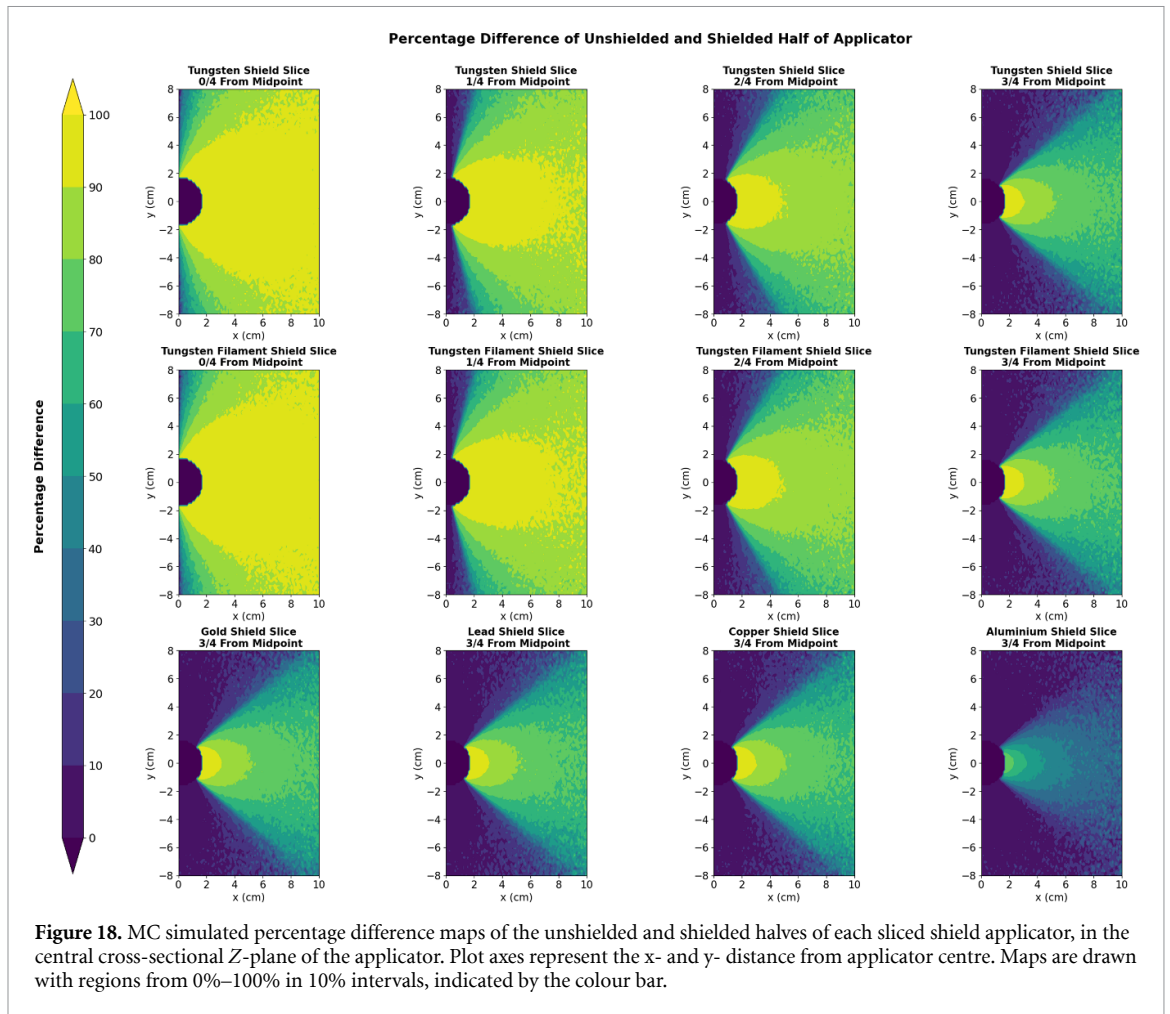
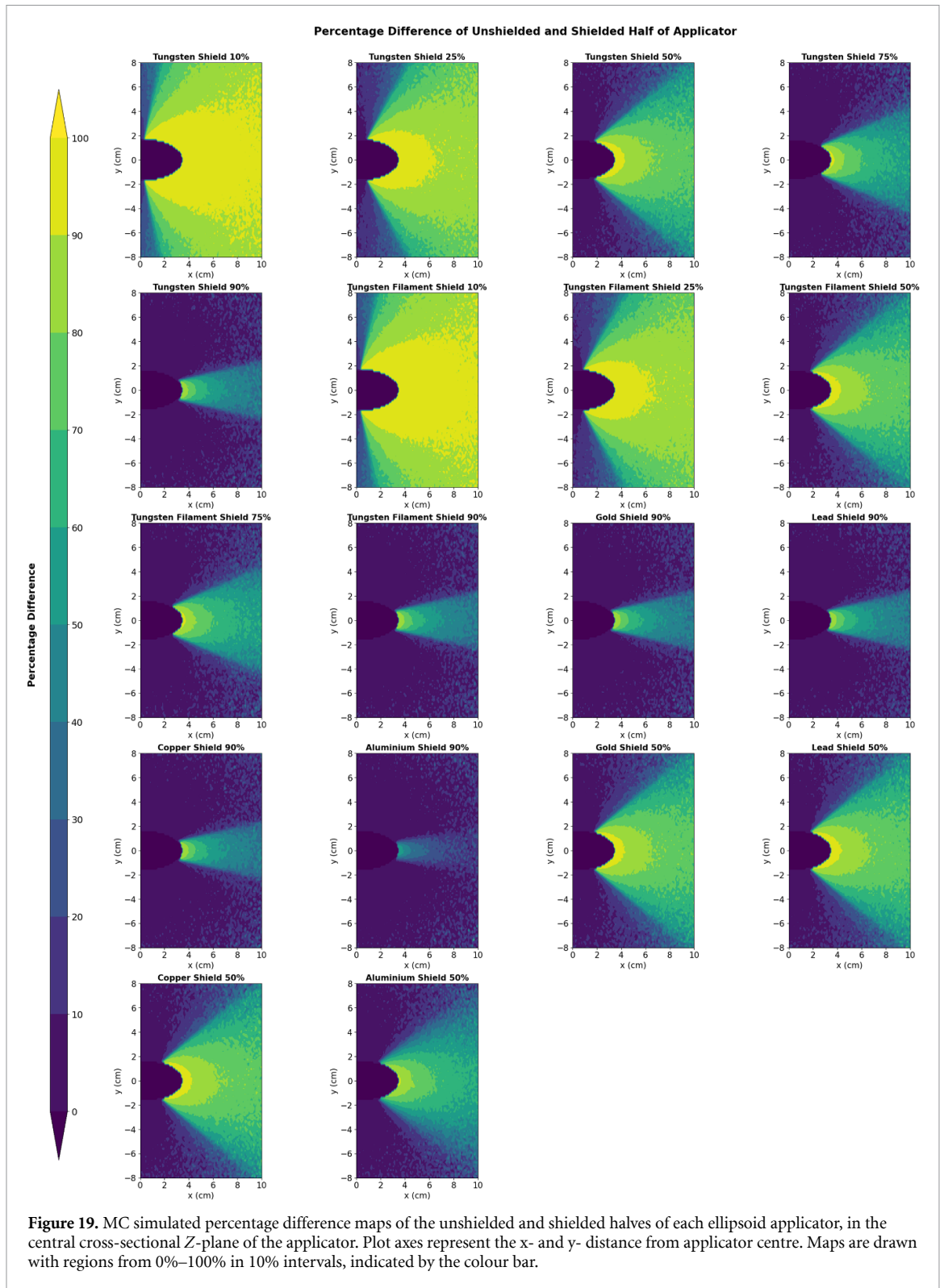


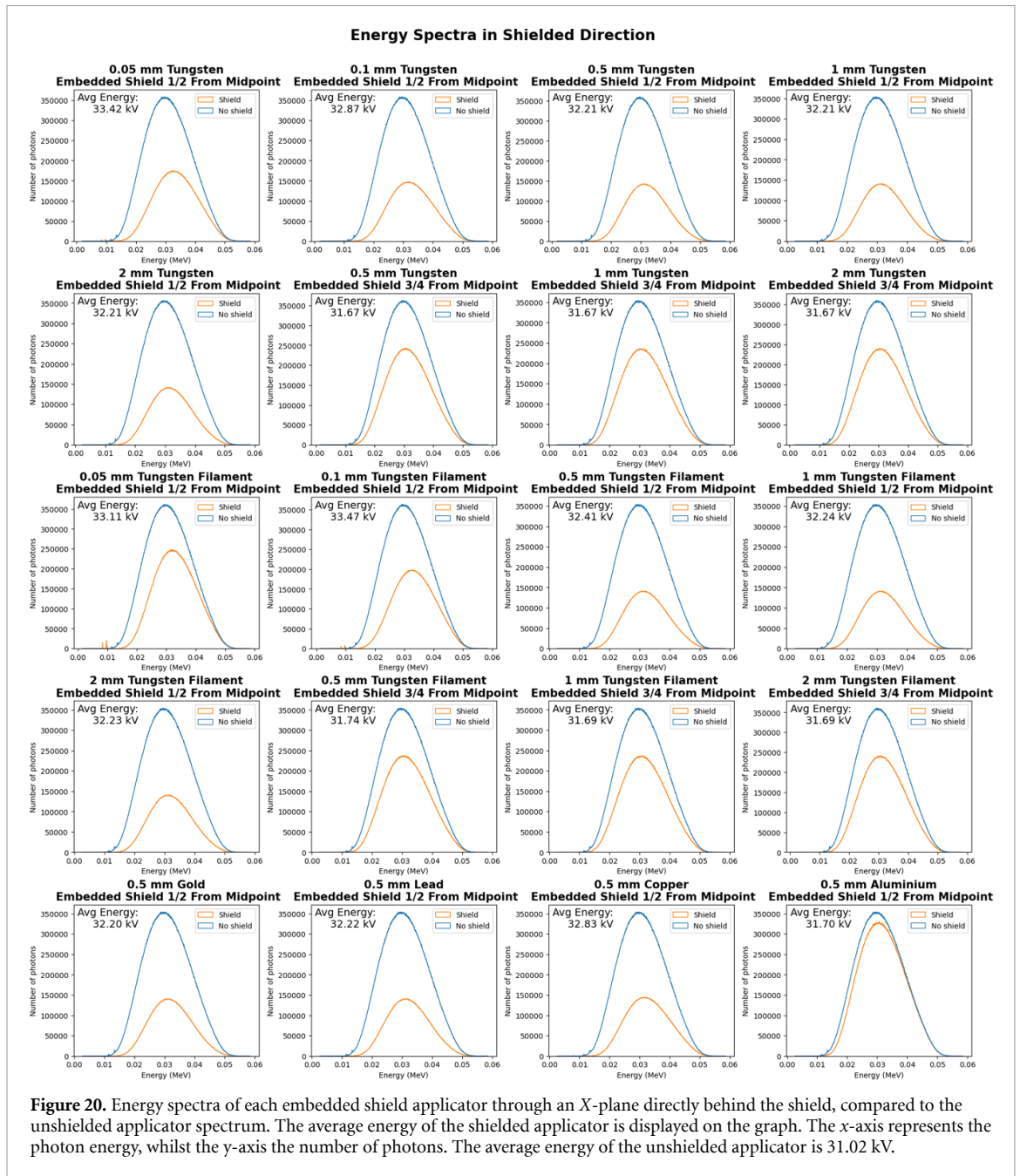
Table 5. MC error for each applicator from which PDDs are produced, along with the R2 value of each fitted MC PDD curve.

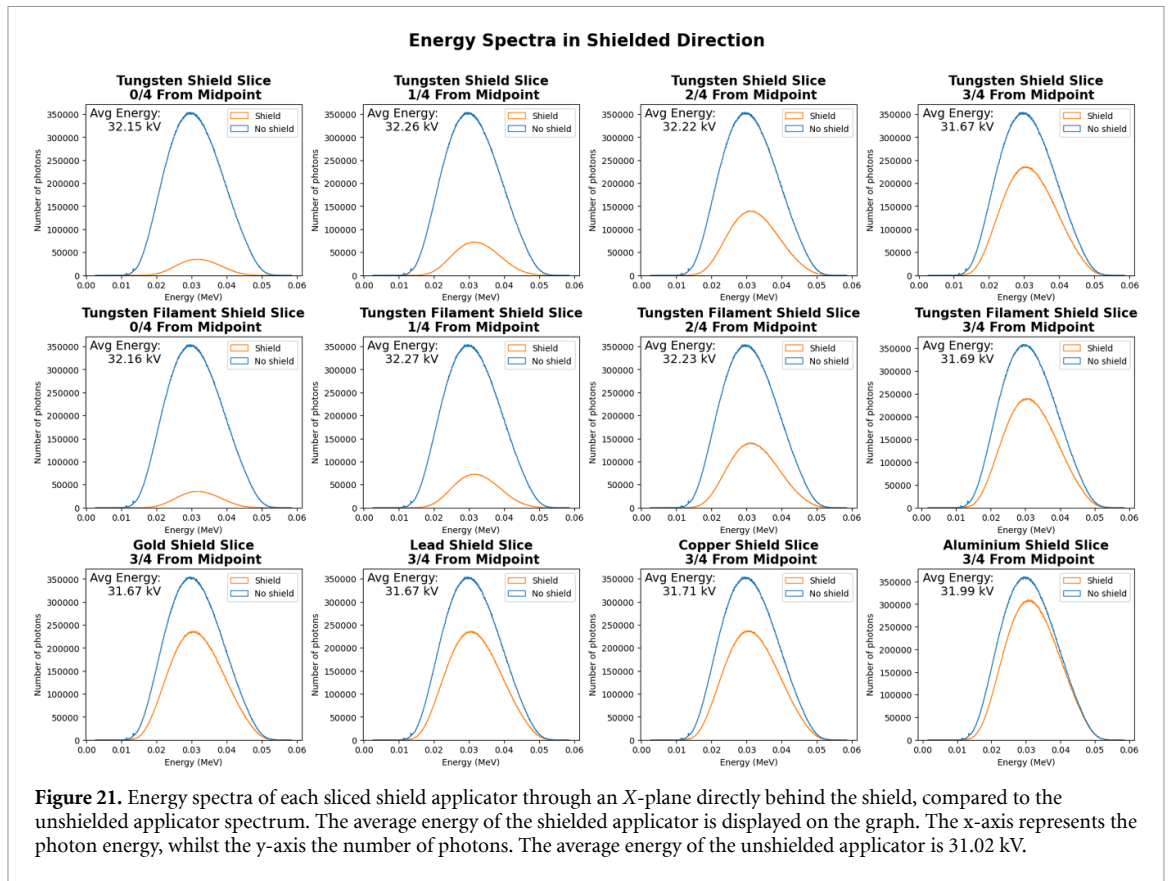
Applicator	Maximum MC error (%)	R ²
No shield	1.4752	0.9999
0.05 mm Tungsten Filament Shield 1/2 From Midpoint	0.8723	0.9997
0.1 mm Tungsten Filament Shield 1/2 From Midpoint	0.6245	0.9995
0.5 mm Tungsten Filament Shield 1/2 From Midpoint	0.2192	0.9958
1 mm Tungsten Filament Shield 1/2 From Midpoint	0.2031	0.9940
2 mm Tungsten Filament Shield 1/2 From Midpoint	0.2000	0.9949
0.5 mm Tungsten Filament Shield 3/4 From Midpoint	0.2991	0.9981
1 mm Tungsten Filament Shield 3/4 From Midpoint	0.2854	0.9973
2 mm Tungsten Filament Shield 3/4 From Midpoint	0.2851	0.9972
0.5 mm Tungsten Shield 1/2 From Midpoint	0.2026	0.9934
0.5 mm Gold Shield 1/2 From Midpoint	0.1970	0.9937
0.5 mm Lead Shield 1/2 From Midpoint	0.1973	0.9943
0.5 mm Copper Shield 1/2 From Midpoint	0.2875	0.9965
0.5 mm Aluminium Shield 1/2 From Midpoint	1.3083	0.9998
Tungsten Filament Shield Slice 0/4 From Midpoint	0.0905	0.9507
Tungsten Filament Shield Slice 1/4 From Midpoint	0.1408	0.9795
Tungsten Filament Shield Slice 2/4 From Midpoint	0.2016	0.9935
Tungsten Filament Shield Slice 3/4 From Midpoint	0.2814	0.9973
Tungsten Shield Slice 3/4 From Midpoint	0.2858	0.9963
Gold Shield Slice 3/4 From Midpoint	0.2829	0.9979
Lead Shield Slice 3/4 From Midpoint	0.2855	0.9963
Copper Shield Slice 3/4 From Midpoint	0.2864	0.9969
Aluminium Shield Slice 3/4 From Midpoint	0.7982	0.9997
No Shield Ellipsoid	3.6014	0.9996
Tungsten Filament Shield 10%	0.4943	0.9291
Tungsten Filament Shield 25%	0.6317	0.9655
Tungsten Filament Shield 50%	0.9114	0.9819
Tungsten Filament Shield 75%	1.1465	0.9899
Tungsten Filament Shield 90%	1.3928	0.9957
Tungsten Shield 50%	0.8859	0.9886
Gold Shield 50%	0.9210	0.9813
Lead Shield 50%	0.9035	0.9859
Copper Shield 50%	0.8916	0.9853
Tungsten Shield 50%	1.2125	0.9904

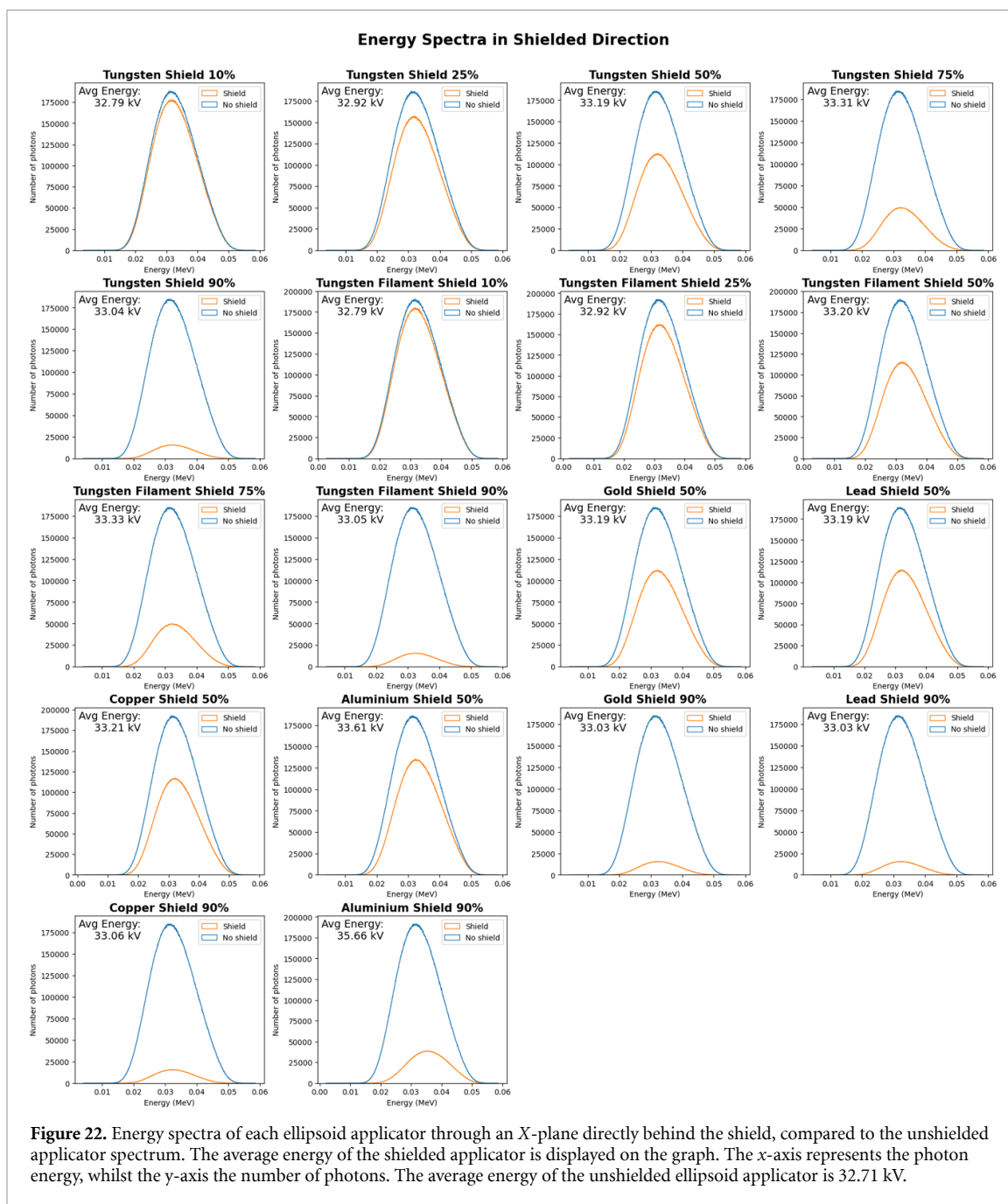












ORCID iDs

Xavier Jones  <https://orcid.org/0009-0004-1234-3980>
 Gabor Neveri  <https://orcid.org/0009-0003-6148-6462>
 Marsha Chin  <https://orcid.org/0000-0002-2463-5970>
 Pejman Rowshanfarzad  <https://orcid.org/0000-0001-8306-7742>

References

- AG CZM 2022 Intrabeam 600 technical specifications (available at: www.zeiss.com/medtec/us/c/iort/zeiss-intrabeam-600.html) (Accessed 9 October 2024)
- Alvarez D S A, Watson P G F, Popovic M, Heng V J, Evans M D C and Seuntjens J 2021 Monte carlo calculation of the tg-43 dosimetry parameters for the intrabeam source with spherical applicators *Phys. Med. Biol.* **66** 215017
- Alvarez D S, Watson P G, Popovic M, Jean Heng V, Evans M D C and Seuntjens J 2020 Monte carlo calculation of the relative tg-43 dosimetry parameters for the intrabeam electronic brachytherapy source *Phys. Med. Biol.* **65** 245041
- Bouزيد D, Bert J, Dupre P F, Benhalouche S, Pradier O, Bousson N and Visvikis D 2015 Monte-carlo dosimetry for intraoperative radiotherapy using a low energy x-ray source *Acta Oncol.* **54** 1788–95

- Calvo F A, Sole C V, Rutten H J, Dries W J, Lozano M A, Cambeiro M, Poortmans P and González-Bayón L 2020 ESTRO/ACROP IORT recommendations for intraoperative radiation therapy in locally recurrent rectal cancer *Clin. Transl. Radiat. Oncol.* **24** 41–48
- Chin M 2022 Dosimetric evaluation of an intraoperative radiotherapy system: a measurement-based and monte carlo modelling investigation *Master's Thesis* University of Western Australia
- Chin M, Rowshanfarzad P, Neveri G, Ebert M A and Pfefferlé D 2023 Dosimetric evaluation of an intraoperative radiotherapy system: a measurement-based and Monte-Carlo modelling investigation *Phys. Eng. Sci. Med.* **46** 687–701
- Clausen S, Schneider F, Jahnke L, Fleckenstein J, Hesser J, Glatting G and Wenz F 2012 A monte carlo based source model for dose calculation of endovaginal target brachytherapy with intrabeam and a cylindrical applicator *Z. Med. Phys.* **22** 197–204
- Conte B, Casey D L, Tringale K R, LaQuaglia M P, Gerstle J T, Wexler L, Ortiz M V and Wolden S L 2024 Intraoperative radiation therapy for pediatric sarcomas and other solid tumors *Pediatr. Blood Cancer* **71** e30949
- Devic S, Aldelaijan S, Mohammed H, Tomic N, Liang L H, DeBlois F and Seuntjens J 2010 Absorption spectra time evolution of ebt-2 model gafchromic™ film *Med. Phys.* **37** 2207–14
- Eaton D J and Duck S 2010 Dosimetry measurements with an intra-operative x-ray device *Phys. Med. Biol.* **55** N359–69
- Ebert M A and Carruthers B 2003 Dosimetric characteristics of a low-kv intra-operative x-ray source: implications for use in a clinical trial for treatment of low-risk breast cancer *Med. Phys.* **30** 2424–31
- FormFutura 2019 Technical data sheet product name: volcano pla (available at: <https://formfutura.com/datasheets/formfutura-tds-volcanopla.pdf>) (Accessed 27 March 2024)
- FormFutura 2024 Volcano pla (available at: <https://formfutura.com/product/volcano-pla/>) (Accessed 11 March 2024)
- Grimm A, Wollmann E, Sperk E, Weiß C, Sütterlin M, Berlit S and Tuschy B 2024 Intraoperative radiotherapy (IORT) of early breast cancer with low-energy x-rays in breast-conserving surgery *Strahlenther. Onkol.* **200** 296–305
- Gunderson L L, Willett C G, Calvo F A and Harrison L B 2011 *Intraoperative Irradiation: Techniques and Results* (Springer)
- Kawrakow I et al 2000 Egsnrc toolkit for Monte Carlo simulation of ionizing radiation transport [Release v2023] (<https://doi.org/10.4224/40001303>)
- Kawrakow I, Rogers D W O, Mainegra-Hing E, Tessier F and Walters B 2023 The egsnrc code system: monte carlo simulation of electron and photon transport *Report, National Research Council Canada*
- Kyrgias G, Hajioannou J, Tolia M, Kouloulis V, Lachanas V, Skoulakis C, Skarlatos I, Rapisda A and Bizakis I 2016 Intraoperative radiation therapy (IORT) in head and neck cancer: a systematic review *Medicine* **95** e5035
- Moradi F, Ung N M, Khandaker M U, Mahdiraji G A, Saad M, Abdul Malik R, Bustam A Z, Zaili Z and Bradley D A 2017 Monte carlo skin dose simulation in intraoperative radiotherapy of breast cancer using spherical applicators *Phys. Med. Biol.* **62** 6550–66
- Nwankwo O, Clausen S, Schneider F and Wenz F 2013 A virtual source model of a kilo-voltage radiotherapy device *Phys. Med. Biol.* **58** 2363–75
- Papaconstadopoulos P, Hegyi G, Seuntjens J and Devic S 2014 A protocol for ebt3 radiochromic film dosimetry using reflection scanning *Med. Phys.* **41** 122101
- Pilar A, Gupta M, Laskar S and Laskar S G 2017 Intraoperative radiotherapy: review of techniques and results *Ecancermedicalscience* **11** 750
- Schneider F, Clausen S, Tholking J, Wenz F and Abo-Madyan Y 2014 A novel approach for superficial intraoperative radiotherapy (iort) using a 50 kv x-ray source: a technical and case report *J. Appl. Clin. Med. Phys.* **15** 4502
- Sethi A, Emami B, Small W and Thomas T O 2018 Intraoperative radiotherapy with intrabeam: technical and dosimetric considerations *Front. Oncol.* **8** 74
- Shamsabadi R, Baghani H R, Azadegan B and Mowlavi A A 2020 Monte Carlo based analysis and evaluation of energy spectrum for low-kv iort spherical applicators *Z. Med. Phys.* **30** 60–69
- Shamsabadi R, Baghani H R, Mowlavi A A and Azadegan B 2021 Effective energy assessment during breast cancer intraoperative radiotherapy by low-energy x-rays: a monte carlo study *Radiat. Environ. Biophys.* **60** 125–34
- The Virtual Foundry 2024 Rapid 3dshield tungsten filament (available at: <https://shop.thevirtualfoundry.com/en-au/products/rapid-3dshield-tungsten-filament?variant=29394884952147>) (Accessed 1 May 2024)
- Villarreal-Barajas J E and Khan R F 2014 Energy response of EBT3 radiochromic films: implications for dosimetry in kilovoltage range *J. Appl. Clin. Med. Phys.* **15** 4439
- Watson P G F, Bekerat H, Papaconstadopoulos P, Davis S and Seuntjens J 2018 An investigation into the intrabeam miniature x-ray source dosimetry using ionization chamber and radiochromic film measurements *Med. Phys.* **45** 4274–86
- Watson P G F, Popovic M and Seuntjens J 2017 Determination of absorbed dose to water from a miniature kilovoltage x-ray source using a parallel-plate ionization chamber *Phys. Med. Biol.* **63** 015016
- Zolfaghari S, Francis K, Kairn T and Crowe S 2017 Commissioning a hobby cutting device for radiochromic film preparation *Australas. Phys. Eng. Sci. Med.* **40** 449–53